NASA/TM-20210021453

Microstructural Observations on Advanced Multilayer Protective Coatings for Nuclear Thermal Propulsion

S.V. Raj and J.A. Nesbitt
Glenn Research Center, Cleveland, Ohio

W. Jennings
HX5, LLC, Brook Park, Ohio

P. Bonacuse
Glenn Research Center, Cleveland, Ohio

October 2021

NASA STI Program . . . in Profile

Since its founding, NASA has been dedicated to the advancement of aeronautics and space science. The NASA Scientific and Technical Information (STI) Program plays a key part in helping NASA maintain this important role.

The NASA STI Program operates under the auspices of the Agency Chief Information Officer. It collects, organizes, provides for archiving, and disseminates NASA's STI. The NASA STI Program provides access to the NASA Technical Report Server—Registered (NTRS Reg) and NASA Technical Report Server—Public (NTRS) thus providing one of the largest collections of aeronautical and space science STI in the world. Results are published in both non-NASA channels and by NASA in the NASA STI Report Series, which includes the following report types:

- TECHNICAL PUBLICATION. Reports of completed research or a major significant phase of research that present the results of NASA programs and include extensive data or theoretical analysis. Includes compilations of significant scientific and technical data and information deemed to be of continuing reference value. NASA counter-part of peer-reviewed formal professional papers, but has less stringent limitations on manuscript length and extent of graphic presentations.

- TECHNICAL MEMORANDUM. Scientific and technical findings that are preliminary or of specialized interest, e.g., “quick-release” reports, working papers, and bibliographies that contain minimal annotation. Does not contain extensive analysis.

- CONTRACTOR REPORT. Scientific and technical findings by NASA-sponsored contractors and grantees.

- CONFERENCE PUBLICATION. Collected papers from scientific and technical conferences, symposia, seminars, or other meetings sponsored or co-sponsored by NASA.

- SPECIAL PUBLICATION. Scientific, technical, or historical information from NASA programs, projects, and missions, often concerned with subjects having substantial public interest.

- TECHNICAL TRANSLATION. English-language translations of foreign scientific and technical material pertinent to NASA's mission.

For more information about the NASA STI program, see the following:

- Access the NASA STI program home page at http://www.sti.nasa.gov

- E-mail your question to help@sti.nasa.gov

- Fax your question to the NASA STI Information Desk at 757-864-6500

- Telephone the NASA STI Information Desk at 757-864-9658

- Write to:
  NASA STI Program
  Mail Stop 148
  NASA Langley Research Center
  Hampton, VA 23681-2199

NASA/TM-20210021453

Microstructural Observations on Advanced Multilayer Protective Coatings for Nuclear Thermal Propulsion

S.V. Raj and J.A. Nesbitt
Glenn Research Center, Cleveland, Ohio

W. Jennings
HX5, LLC, Brook Park, Ohio

P. Bonacuse
Glenn Research Center, Cleveland, Ohio

National Aeronautics and
Space Administration

Glenn Research Center
Cleveland, Ohio 44135

October 2021

Acknowledgments

The specimens were coated by Mr. Victor Arrieta and Mr. Brian Williams at Ultramet, Pacoma, CA under NASA contract PO 80GRC017P0012. The authors thank Mr. Rick Rauser for making the m-CT scan measurements, Mr. John Setlock for conducting the thermal cycling tests, Mr. Raymond Babuder for sectioning the specimens, and Ms. Joy Buehler for metallographic preparation of the specimens. Dr. Amjad Almansour reviewed this report, and his comments and suggestions are gratefully acknowledged. This work was supported by NASA's Space Technology Mission Directorate (STMD) through the Space Nuclear Propulsion (SNP) project.

Level of Review: This material has been technically reviewed by technical management.

Available from

NASA STI Program
Mail Stop 148
NASA Langley Research Center
Hampton, VA 23681-2199

National Technical Information Service
5285 Port Royal Road
Springfield, VA 22161
703-605-6000

This report is available in electronic form at http://www.sti.nasa.gov/ and http://ntrs.nasa.gov/

Microstructural Observations on Advanced Multilayer Protective Coatings for Nuclear Thermal Propulsion

S.V. Raj and J.A. Nesbitt[*]
National Aeronautics and Space Administration
Glenn Research Center
Cleveland, Ohio 44135

W. Jennings
HX5, LLC
Brook Park, Ohio 44142

P. Bonacuse
National Aeronautics and Space Administration
Glenn Research Center
Cleveland, Ohio 44135

Abstract

The present research discusses the microstructures of a new multilayered coating concept proposed to solve the “midrange corrosion” problem observed in NbC and ZrC-coated graphite (Gr) nuclear fuels during the NERVA/Rover programs. The concept envisions designing a compliant multilayered coatings architecture to accommodate the thermal expansion mismatch strains between the ZrC outer coating and the Gr/(U,Zr)C fuel matrix along with using a diffusion barrier to minimize carbon and hydrogen diffusion, respectively. Multilayered coatings were deposited on Gr substrates by chemical vapor deposition (CVD). Graphite disks, as well as the inner channels of a 19-hole hexagonal rod 152.4 mm long, were coated by CVD in proof-of concept process demonstration studies. Coated disk specimens were thermally-cycled between ambient and 1900 K for as long as 20 cycles with a 1 h hold time at the temperature using both stepped and non-interrupted thermal cycling methods. Detailed cross-sectional microstructural analyses were conducted on the thermally-cycled coated disks. These results showed that the coatings were intact after 20 thermal cycles at 1900 K although the bonding of the overlay Mo coating appeared to be influenced by the oxygen content in the layer. Seven transverse sections were cut along the length from the coated hexagonal rod for microstructural studies. All the 19 channels were observed to have been coated in all the sections. This paper reports the results of detailed microstructural analyses, compositional line scans and EDS maps conducted on three coated channels from a mid-section of the rod. The measured values of carbon (C) were observed to be exceptionally high in all the specimens, which were attributed to hydrocarbon contamination of the specimen surfaces. It was observed that the oxygen (O) levels were high in all the coating layers even after approximately correcting for the observed high values of C. The source of O contamination of the CVD reactor system was attributed to either the presence of oxychloride impurities in the precursor salts or a pin hole leak in the coating system. It is concluded that high values of O result in poor bonding of the Mo overlay to the ZrC layer. These trials have established that it is possible to deposit multilayered coatings by CVD in 19-hole hexagonal rods 152.4 mm long similar to the NERVA fuel rod design although the quality of the coatings and the uniformity of their thicknesses require further improvement.

---

[*] Currently retired.

1.0 Introduction

Faster space travel and a manned mission to Mars require the development of advanced nuclear propulsion systems to ensure that the astronauts can return relatively quickly and safely to Earth to minimize exposures to deep space radiation [1,2,3]. A nuclear thermal propulsion (NTP) rocket has about twice the specific impulse of a H_2/O_2 chemical rocket, which makes it attractive for deep space manned missions to Mars and other celestial bodies [4,5,6]. The Nuclear Engine for Rocket Vehicle Application (NERVA) and Rover programs demonstrated the viability of NTP engines in several ground tests conducted between 1959 and 1972 [5]. Extensive studies were conducted during the NERVA/Rover programs to develop chemical vapor deposited (CVD) process methodologies and parameters to coat 19-channeled (U,Zr)C/Gr nuclear fuel rods as long as 1320 mm with either NbC or ZrC [5,6,7,8,9,10,11, 12,13]. Most of the nominal coating compositions were stoichiometric NbC although towards the end of the programs, the nominal coating composition was changed to stoichiometric ZrC because of its greater observed resistance to hot hydrogen attack [10,11]. During the NERVA/Rover programs, it was observed that the NTP engine life was severely limited by "mid-passage" corrosion (MPC) of the graphite (Gr)-based nuclear fuel, where cracks in either the CVD NbC or ZrC coatings allowed the hot hydrogen propellant to react with the Gr substrate to form hydrocarbon reaction products [14,15,16,17,18]. The cracks in the coatings were attributed to differences in the coefficients of thermal expansion (CTE) between the carbide coating and the (U,Zr)C/Gr substrate [10,11]. It was concluded that addressing the MPC problem was key to the successful development of a Gr-based nuclear-fueled NTP engine [14].

Although the NERVA/Rover programs were terminated in 1972, the National Aeronautics and Space Administration's (NASA) Advanced Exploration Systems (AES) division revived a new Gr-based nuclear fuel development effort in 2012 to develop NTP technologies for its planned mission to Mars [2,3]. In the latter case, the research was conducted under a joint NASA-DOE research effort, where the Oak Ridge National Laboratory (ORNL) was responsible for the fuel and coating development effort. In an attempt to reproduce the NERVA/Rover fuel and coating technologies, ORNL fabricated 4-channeled HfO_2/ZrC/Gr[1] extruded hexagonal rods 406.4 mm long [19,20]. The inner surfaces of the channels were CVD coated with a ZrC coating [21]. One ZrC-coated rod was successfully fabricated and tested under pressurized hot hydrogen ultrahigh temperature facility at NASA's Marshall Space Flight Center's (MSFC) Nuclear Thermal Rocket Element Environmental Simulator (NTREES) at various operating conditions [22]. However, the MPC issue was not resolved in the ORNL study.

A separate research study was undertaken at NASA's Glenn Research Center (GRC) under the same AES program to develop multilayer coating architectures to mitigate the MPC problem. The coating architectures and deposition concepts were developed by NASA GRC [23,24], while the processing parameters and methodologies were developed in collaboration with NASA GRC researchers by external vendors under contract with NASA GRC. An earlier report described initial attempts to deposit multilayered coatings on Gr disk specimens in the first proof-of-concept processing investigation [25]. Unfortunately, air leakage in the CVD reactor appeared to have contributed to the high oxygen levels observed in the coating layers resulting in coating debonding and large microstructural variations in coating quality. This earlier work was extended under a different contract issued to Ultramet Advanced Materials Solutions (Ultramet), Pacoima, CA, to develop and optimize coating deposition parameters and methodologies to coat 25.4 mm dia. Gr disks in proof-of-concept studies. Once the process parameters and deposition methodologies had been developed and optimized, the contract was extended to develop the process parameters and deposition methodologies to coat 19 channels machined in hexagonal Gr rods 152.4 mm long and 19.05 mm wide flat-to-flat to represent the geometrical configuration of a

---

[1] HfO_2 was used as a surrogate for UO_2 [20].

NERVA/Rover fuel element. The objectives of the present paper are to report the detailed microstructural studies conducted on these coated specimens.

2.0 Coating Architectural Design

In order to mitigate the MPC problem in a Gr-based nuclear-fueled NTP engine, the coating architecture must fulfill the following critical requirements: (a) The elements[2] in the coating architecture must possess low neutron absorption cross-sections, σ_a; (b) possess high absolute melting temperatures, T_m, significantly above the operating temperature of the NTP engine; (c) diminish and accommodate any CTE mismatch thermal stresses with a compliant layer; and (d) minimize or prevent the outward carbon (C) diffusion from the Gr substrate as well as the inward hydrogen diffusion towards the substrate.

As noted above, an important factor that must be considered in determining the composition of the compliant layer for a NTP engine is the effect of the coating architecture on the neutronics. Figure 1 shows the variation of σ_a for elements with $\sigma_a < 20$ barns [26,27,28] against T_m [29] for several elements in order to identify elements that satisfy (a) and (b) above. The two vertical broken lines represent the range of temperatures in which the NTP engines were tested during the NERVA/Rover programs. The horizontal broken line is the value of $\sigma_a = 2.48$ barns for Mo [26,27] although a value of 2.51 to 2.55 barns has also been reported [28]. An examination of Figure 1 reveals that only C, Mo and Nb have values of $\sigma_a \leq 2.48$ barns and $T_m > 2700$ K. In addition to using these elements in elemental form, their carbides and nitrides would have acceptable values of σ_a and $T_m > 2700$ K. In contrast, only ZrC and ZrN have $T_m > 2700$ K so that carbides and nitrides of Si and Y would not be suitable for use in a NTP coating architecture although they may possess low values of σ_a.

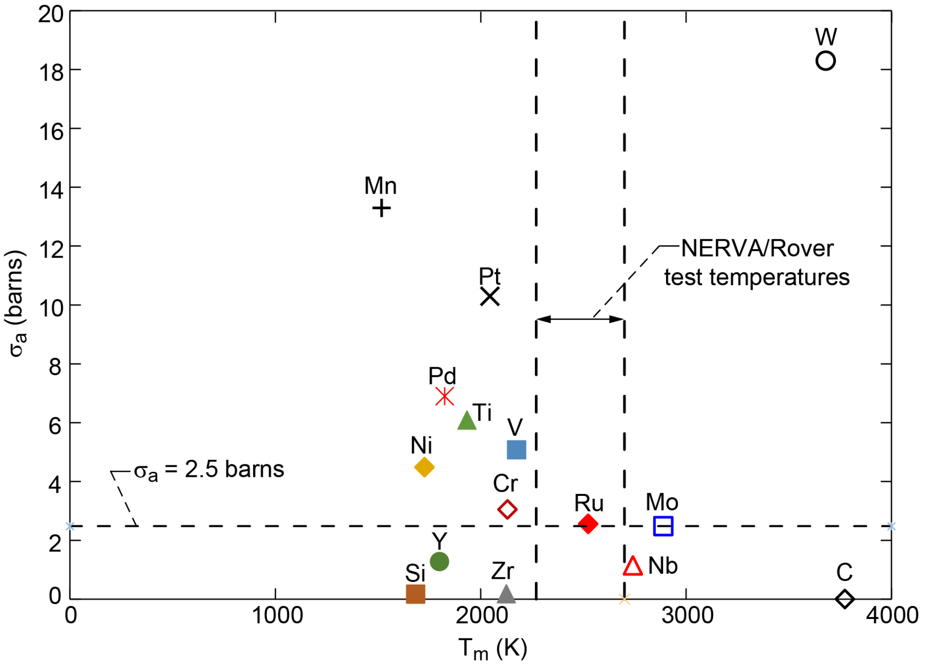

Figure 1.—Plot of the thermal neutron absorption cross-section [26,27,28] against absolute melting temperature [29] for some elements with $\sigma_a < 20$ barns.

---

[2] It is implicitly assumed that the isotopes of these elements with low values of σ_a are commonly available in nature without any need for isotope enrichment.

Figure 2 shows a plot of the thermal strain, $\Delta L/L_0$, where ΔL is the thermal expansion and L_0 is the original specimen length, as a function of the absolute temperature, T, for several carbides (Mo_2C, NbC, UC and ZrC) [30], Mo [31], Nb [31], Nb-25(wt.%))Mo[3], Nb-50%Mo and Nb-75%Mo solid solution alloys [32], and GrafTech XTE 70[4] Gr [33]. As evident in Figure 2, the thermal strains of Nb, Nb-25% Mo, Nb-50%Mo, NbC, UC and ZrC are significantly larger than Gr with the differences in the $\Delta L/L_0$ increasing with increasing T. In contrast, Mo and Mo_2C have similar values of $\Delta L/L_0$ between 300 and 2200 K. The data for the Nb-75%Mo alloy lies in between those for Gr and NbC and ZrC. Clearly, a Nb-75%Mo would be ideally suited to act as a compliant layer to accommodate any mismatch in the thermal strains between the Gr, and either the NbC or ZrC topcoat. Additionally, a Nb-75%Mo compliant layer is unlikely to significantly affect the neutronics while being able to withstand the ultrahigh temperature environment of a NTP engine (Figure 2).

Figure 3 shows the conceptual design of the multilayered coating architecture developed and studied in this investigation [23]. As shown in Figure 3, the multilayer coating architecture: Gr/NbC (or ZrC)/Mo/Nb/ZrC/Mo. The purpose of the NbC or a ZrC diffusion barrier layer next to the Gr substrate is to minimize the outward diffusion of carbon from the substrate and to fill the pores in the substrate. Although Mo_2C was originally considered for use as a carbon diffusion barrier due to its close CTE match with Gr (Figure 2) [23], later analyses of compiled literature data from several sources showed that carbon diffusion in Mo_2C is much faster than in NbC [32]. As shown in Figure 2, a Nb-75%Mo alloy composition is likely to act as an effective compliant layer between the ZrC top layer and the Gr substrate. Since it is difficult to deposit this precise alloy composition by CVD, it is necessary to deposit

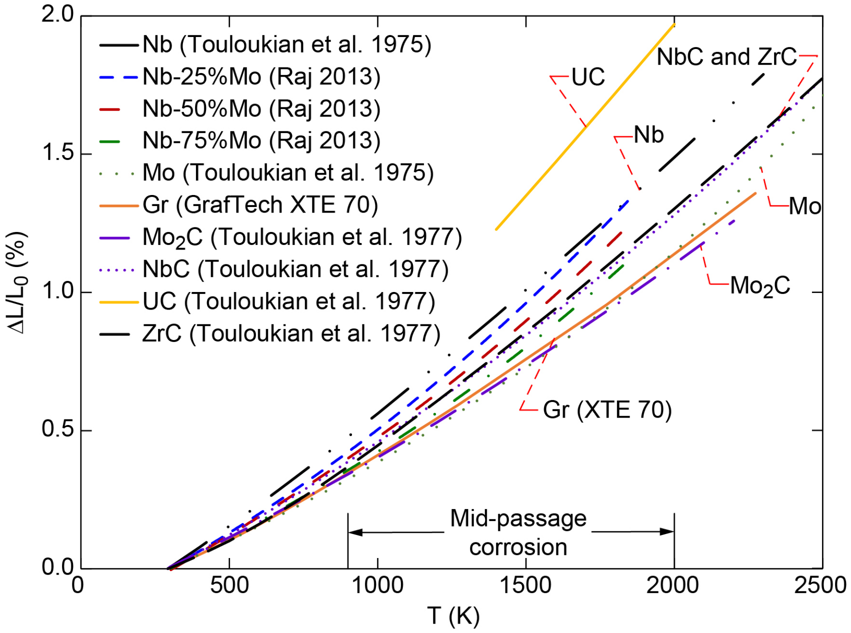

Figure 2.—Plot of longitudinal strain due to thermal expansion against absolute temperature for XTE 70 Gr [33], Mo [31], Nb [31], Nb-Mo alloys [32], Mo_2C [30], NbC [30], UC [30] and ZrC [30].

---

[3] Unless otherwise stated, all alloy compositions are reported in wt.% in this paper.

[4] Trademark of GrafTech International, Brooklyn Heights, OH. The $\Delta L/L_0$ values were extracted from the CTE data provided to the author.

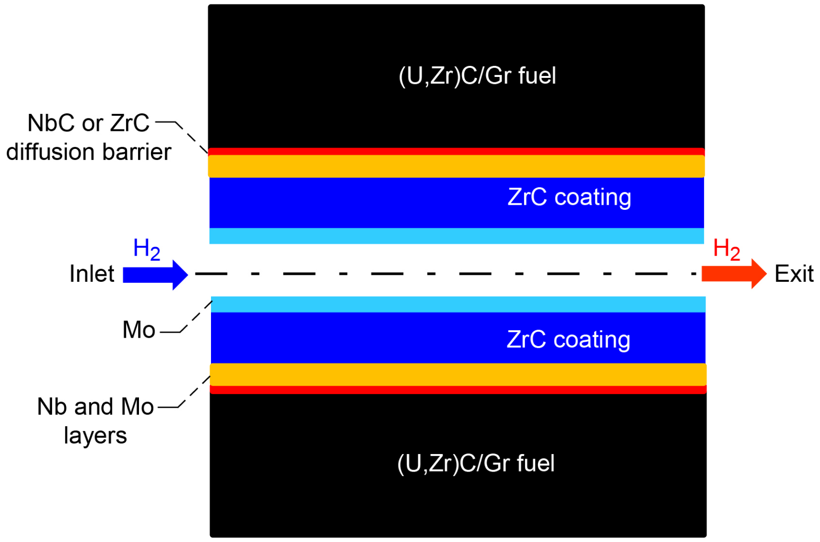

Figure 3.—Proposed coating architecture to protect NERVA/Rover Gr-based fuels from hot hydrogen attack in the mid-band corrosion region of the fuel element [23].

Mo and Nb layers in the appropriate thickness ratio to form the initial coating architecture. The fact that the Mo-Nb binary phase diagram is isomorphous [34], it is expected that Mo and Nb will diffuse into each other at high temperatures to form a Nb-Mo alloy with a composition as close as possible to Nb-75%Mo. Lastly, a ZrC (or NbC) top layer adjacent to the Nb layer is further coated with a Mo overlayer to fill in any cracks in the ZrC and to act as a diffusion barrier against the inward diffusion of hydrogen towards the substrate. These Mo overlay coatings on either a NbC or ZrC top layer were shown to increase coating durability during NTP engine tests in the NERVA/Rover programs [8,11,17].

There are two ways in which the coated-substrate system shown in Figure 3 can be fabricated (Figure 4). Figure 4(a) schematically shows the traditional way in which one or more coating layers are deposited on a channeled substrate, which is termed as the “outside-in” method in this paper. In this method, the deposited layers bond to the substrate and the surface of the coating moves inwards towards the axis of the channel as the coating thickness increases during deposition. In contrast, Figure 4(b) schematically demonstrates the “inside-out” method, where the coating layers are deposited on either a permanent or a sacrificial cylindrical mandrel where the Mo overlayer diffusion bonds to it. In this case, the surface of the coating moves outwards away from the mandrel axis as the coating thickness increases. The coated mandrel is then inserted into pre-drilled channels in the substrate and diffusion bonded to it before either drilling out or preferentially etching out the mandrel. It is important to note that the NERVA/Rover programs used the outside-in method, where the coatings were deposited within 19 channels in (U,Zr)C/Gr nuclear fuel rods. The alternative inside-out method has not been fully developed but it offers several potential advantages as well as challenges compared to the outside-in method.

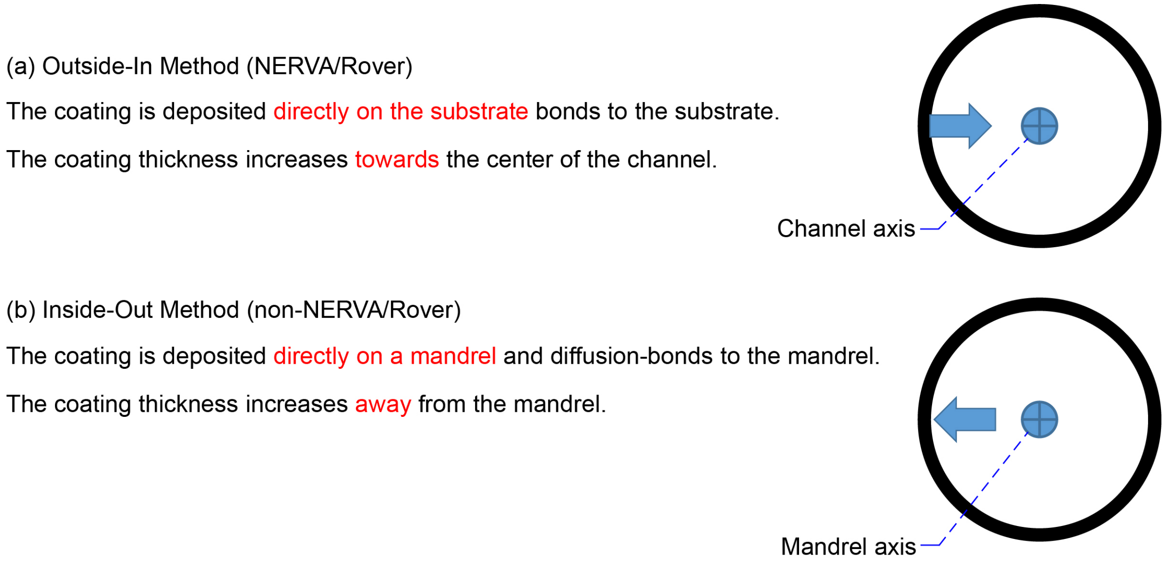

(a) Outside-In Method (NERVA/Rover)

The coating is deposited directly on the substrate bonds to the substrate.

The coating thickness increases towards the center of the channel.

(b) Inside-Out Method (non-NERVA/Rover)

The coating is deposited directly on a mandrel and diffusion-bonds to the mandrel.

The coating thickness increases away from the mandrel.

Figure 4.—Schematic illustrating (a) the NERVA/Rover outside-in and (b) the proposed inside-out methods for coating NTP fuel elements.

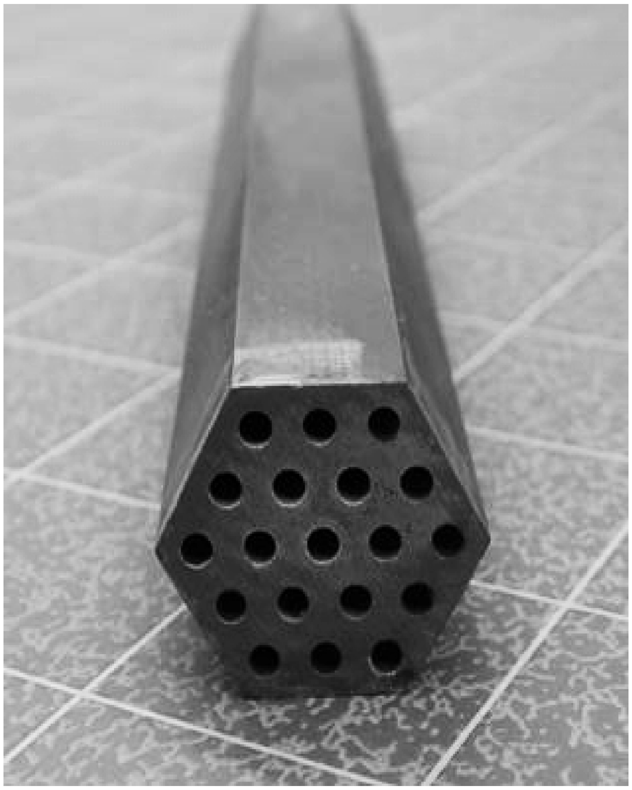

Figure 5.—Photograph of the Mersen 2160 hexagonal rod with 19 channels.

3.0 Experimental Procedures

The Mersen 2160 graphite specimens used in the present investigation were procured in the final machined form from Mersen USA Greenville, MI. The properties of Mersen 2160 are given elsewhere

[35]. The disk specimens were 25.4 mm dia. x 3.2 mm thick, while the 152.4 mm long hexagonal rods with 19.05 mm flat-to-flat width and 19 machined channels each 2.3 mm dia. were similar to the NERVA/Rover fuel elements in cross-section [10] (Figure 5). The R_a surface finish was 64 μm.

As noted earlier, the specimens were CVD coated by Ultramet, Pacoima, CA under contract. One set of disks were coated on one face using the coating architecture: Gr substrate/NbC (15 μm) (diffusion barrier)/Mo (15 μm)/Nb (5 μm)/ZrC (25 to 60 μm)/Mo (5 μm) (overlay coating). The nominal thicknesses of the coating layers are indicated in the parenthesis. A second set of disks were coated with thicker coating layers and with an additional Nb overlay coating between the outer Mo overlay coating and the ZrC layer: Gr substrate/NbC (25 μm) (diffusion barrier)/Mo (30 μm)/Nb (10 μm)/ZrC (60 μm)/ Nb (5 μm)/Mo (20 μm) (overlay coating). Although the disks were intentionally coated only on one face, it was often observed that the coating layers were also deposited on the side surfaces as well as along the edges of the opposite face. The Gr substrate/NbC (15 μm) /Mo (15 μm)/Nb (5 μm)/ZrC (25 to 60 μm)/ Mo (5 μm) coating architecture was used for coating the channels in the 152.4 mm long hexagonal rods, where the gas was allowed to flow from one end face to the other.

The CVD coating deposition process involved several stages. Briefly, the NbC diffusion barrier was deposited by directly reacting niobium pentachloride with graphite substrate

$$NbCl_5\ (g) + C\ (s) \rightarrow NbC\ (s) + 5/2Cl_2\ (g) \quad (1)$$

The deposition of the Mo, Nb and ZrC layers on heated substrates were achieved through the following reactions in a separate reactor chamber:

$$MoCl_5\ (g) + 5/2\ H_2\ (g) \rightarrow Mo\ (s) + 5HCl\ (g) \quad (2)$$

$$NbCl_5\ (g) + 5/2\ H_2\ (g) \rightarrow Nb\ (s) + 5HCl\ (g) \quad (3)$$

$$ZrCl_4\ (g) + CH_4\ (g) \rightarrow ZrC\ (s) + 4HCl\ (g) \quad (4)$$

The molybdenum and niobium pentachlorides, as well as the zirconium tetrachloride, were produced by reacting the corresponding metals with chlorine gas before introducing them into the reactor chamber.

Two as-coated disks, DS-1 and DS-2, were randomly chosen for microstructural observations and thermal cycling studies conducted in a vacuum furnace maintained at vacuum levels of 1.3×10^{-4} to 1.3×10^{-3} Pa (10^{-6} to 10^{-5} torr). Two types of furnace thermal cycling tests were conducted. The first type consisted of several stepped heat-cool thermal cycles of DS-2 between ambient and 1900 K. In this case, a coated disk was heated from room temperature to 1000 K after evacuating the chamber, held at temperature for 1 h, followed by furnace cooling back to room temperature in the first thermal cycle. A section was cut off for microstructural evaluation using a cutting diamond saw operating at a slow cutting speed and water as lubricant to prevent damaging the coating layers[5]. The procedure was repeated for the remaining disk in temperature increments of 100 K until and including 1900 K (i.e., the last cycle was at 1900 K). The last remnant disk was directly thermally cycled between ambient and 1900 K for an additional 9 cycles with 1 h hold times at 1900 K. Thus, the total cumulative thermal cycles were 19 cycles consisting of 10 step cycles between 1000 and 1900 K followed by 9 direct cycles at 1900 K. In the second type of thermal cycling test, DS-1 was directly cycled between ambient and 1900 K for 20 cycles with a 1 h hold time at 1900 K.

---

[5] It is noted that sectioning the specimen will change the stresses in the coating which could affect the durability of the coated specimen. Additionally, there was extensive outgassing during the initial period of each heat-up cycle presumably because of moisture entrapment in the coating layers during the cutting process. As will be discussed in Section 4.1, this entrapped moisture also appears to have attacked the Mo layer (Figure 10(a) to (b), Figure 11(e)).

Figure 6.—Photograph showing the direction of the μ-CT scan from end faces, A and B, of the coated rod up to a distance of 25.4 mm as depicted by the arrows.

Micro-computed tomography (μ-CT) scans were conducted on the coated 152.4 mm long hexagonal coated Gr rod. Figure 6 shows the coated Gr rod with arrows showing the direction of the scans from end faces A and B. The scans were conducted from end faces A and B up to a distance of 25.4 mm at 10 μm voxel intervals between scans. Since a large amount of data were generated, only images taken at locations 0, 6.35, 12.7, 19.1 and 25.4 mm from each face are included in the report.

The disks DS-1 and DS-2 were transversely sectioned with a slow speed diamond rotating saw using water as the lubricating fluid. Identical cutting procedures were also followed for sectioning the 152.4 mm long hexagonal rod. In this case, it was sectioned into six longitudinal and seven transverse sections after vacuum infiltrating the channels with epoxy to protect the coatings from damage during sectioning. Figure 7(a) shows the schematic cut-up diagram, where ‘L’ denotes the longitudinal section and ‘T’ denotes the transverse section. Each section was carefully identified with respect to its location in the rod by numbering the transverse sections from one end to the other as 1T, 2T,…7T, and identifying the longitudinal sections in between two transverse sections as 1-2L, 2-3L,… 6-7L. Most of the microstructural observations were conducted on the transverse sections, where the arrows shown in Figure 7(a) point to the viewing surfaces for microstructural observations. Since the orientation of the cut longitudinal sections were often found to be misaligned with the channel axes, no additional insight could be determined by making observations on these specimens. A matrix nomenclature, R-C, where R is the row and C is the channel number, was used to identify the location of each channel in the cross-section of the transverse sectioned specimens (Figure 7(b)). Thus, 1-1 represents the 1st channel in row 1, 3-3 signifies the 3rd channel in row 3 (i.e., center channel), and 5-2 represents the 2nd channel in row 5.

It is important to identify the location of each channel in specimens 1T to 7T with those in the uncut rod in order to qualitatively correlate the characteristics of the coatings with the CVD process. Therefore, special care was taken after the cutting process to ensure that each channel, R-C, in the transverse sections 1T to 7T corresponded to the same channel running along the length of the hexagonal rod by suitably marking the front and back faces of the transverse section. Additional precautions were taken during the epoxy mounting and polishing of the specimens 1T to 7T by marking the R-C value for each channel on the back of each translucent mount.

Optical and scanning electron microscopy (SEM), back scattered electron (BSE) imaging, energy dispersive spectroscopy (EDS) and compositional line scans were conducted on polished specimens. In this case, the specimens were vibratory polished to its final finish using a 0.05 μm colloidal silica polishing media. The polished specimens were sputtered-coated with a 5 to 10 nm platinum (Pt) layer for SEM observations. High resolution low magnification microstructures of all 19 channels were obtained on a specially equipped optical microscope, as well as on a SEM, to determine whether all the channels

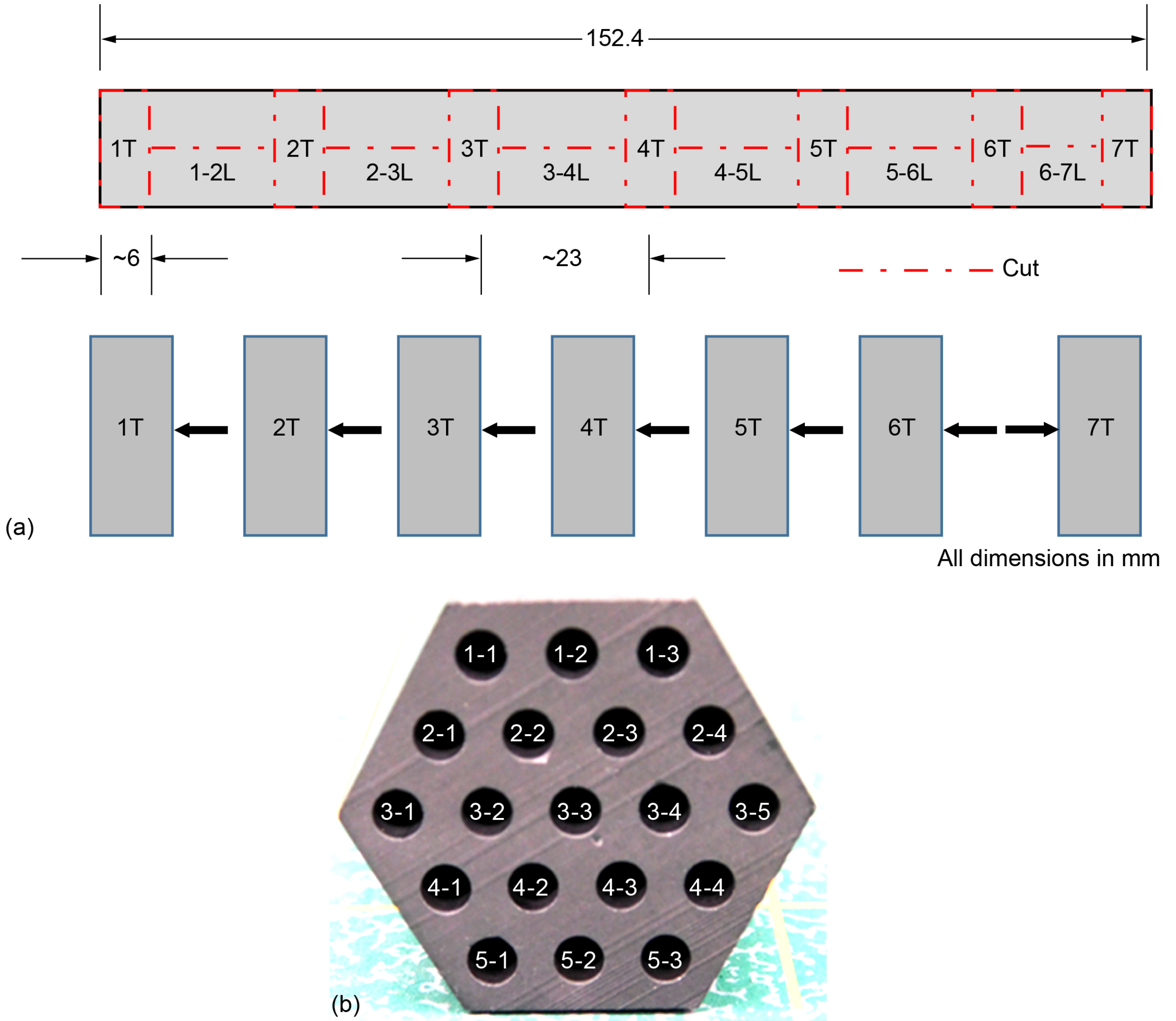

Figure 7.—(a) Schematic of the cutting diagram showing the locations of the longitudinal and transverse metallographic sections with respect to the coated rod. The arrows point to the viewing surfaces. (b) Schematic showing the schema used for identifying each channel with respect to its neighbors on a metallographic cross-sectional specimen, where R and C are row and channel numbers, respectively.

were coated in a specimen. In each specimen, nine channels were examined: 1-1, 1-2, 1-3, 3-1, 3-3, 3-5, 5-1, 5-2, 5-3 (Figure 7(b)). In this case, several microstructural images of each channel were obtained by slowly scanning a pre-defined specimen area covering all the 19 channels over several hours. These images were automatically stitched together by the software to produce an overall image of the specimen cross-section showing all 19 channels. Detailed SEM, BSE, EDS maps and compositional line analyses were conducted only on transverse sections 1T, 4T and 7T (Figure 7(a)).

4.0 Results and Discussion

4.1 Microstructures of As-Received Coated Graphite Disks

Figure 8 shows a macrograph of an as-received coated disk, where it is seen that there is no apparent sign of coating debonding. The cross-sectional microstructures of the two coated disks showed debonding either at the Mo overlay/ZrC interface in DS-1 (Figure 9(a)) or at the NbC/Mo layer in DS-2 (Figure 10(a) to (b)). In specimen DS-1, the microstructural observations revealed that all the deposited layers were well-bonded except for the Mo overlay layer, which had debonded from the ZrC layer (Figure 9(a)). As expected, the NbC diffusion barrier as well as the Mo, Nb and ZrC layers were observed in the cross-sectional microstructures. While the NbC, Mo, and the ZrC were fairly thick, the Nb layer was relatively thin. The coating layer thicknesses and the morphologies of the interfaces were fairly uniform throughout the specimen. All the layers were well-bonded except for the debonded Mo overlay noted earlier. A closer examination of the ZrC layer revealed a two-phase lamellar microstructure within the inner 50 to 60 µm thickness layer before becoming homogeneous in the outer 8 to 10 µm layer (Figure 9(b) to (c)). It appears that the ZrC layers were deposited under partial pressures of C_xH_y and $ZrCl_4$ and temperature conditions corresponding to either the ZrC + C + gas or the ZrC + Zr + gas regions of the CVD pseudo-binary phase diagrams [36].

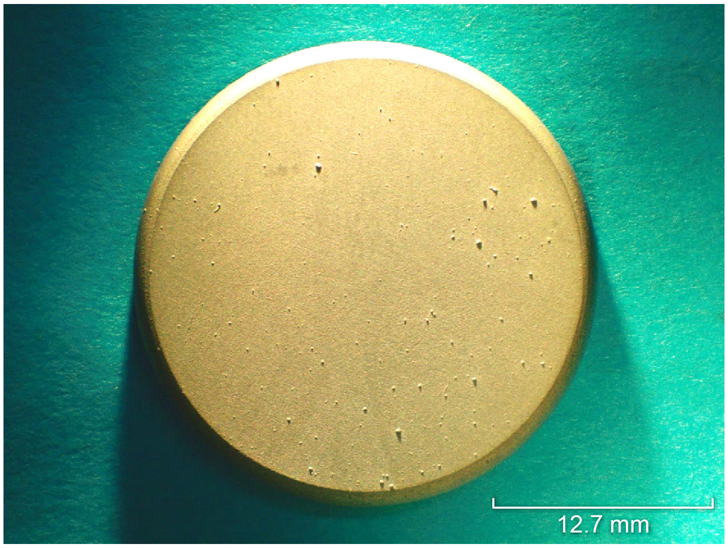

Figure 8.—Macrograph of a coated 25.4 mm diameter Mersen 2160 disk.

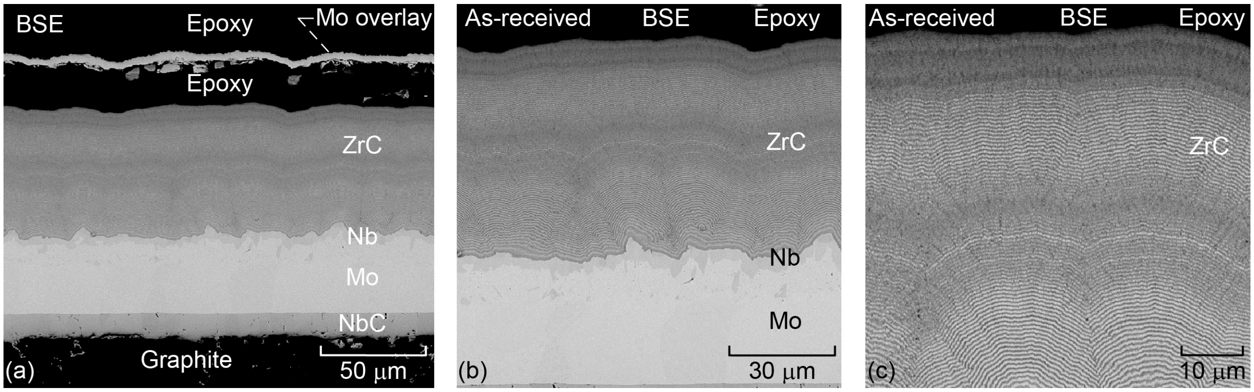

Figure 9.—Back scattered electron images of the cross-sectional microstructures of the as-coated disk specimen, DS-1, showing (a) that all the layers except the Mo overlay were well-bonded. High magnification views of (b) the Mo/Nb/ZrC layers and (c) the ZrC layer showing a transition from a two-phase lamellar microstructure to a single phase microstructure in traversing from the Nb/ZrC interface to the debonded ZrC/Mo overlay interface.

In specimen DS-2, the Mo overlay layer was well-bonded to the ZrC but the NbC diffusion layer had debonded from the Mo layer at the substrate end of the multilayer coating architecture (Figure 10(a)). In another region of this specimen, a debonding crack was observed between the Mo overlay coating and the ZrC layer, where the crack propagated into the ZrC layer and stopped at the ZrC/Nb interface boundary (Figure 10(b)). As expected, the crack did not propagate in the ductile Nb layer. Since one of the concerns of MPC was the relative ease of hydrogen diffusion along vertical cracks in the ZrC coating to the Gr-based nuclear fuel [10,11,17], this observation is significant since it suggests that the rate of hydrogen diffusion to the Gr-based substrate along these through thickness cracks would be minimized by the

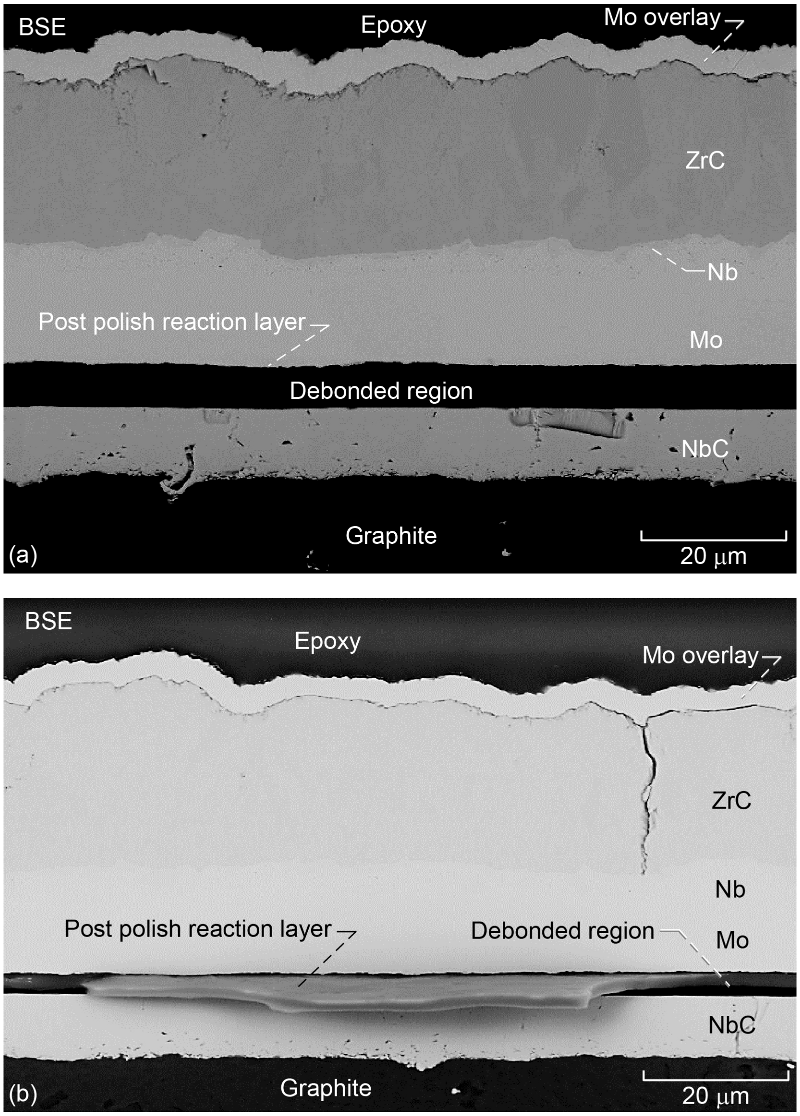

Figure 10.—(a) Back scattered electron image of the cross-sectional microstructures from different locations of the as-coated disk specimen, DS-2, showing that all the layers except the NbC/Mo interface were well-bonded. (b) Isolated cracks observed in the ZrC layer were stopped by the Nb layer. A post-polishing reaction layer was observed in the debonded NbC/Mo interface.

ductile Nb layer. An out-of-plane reaction product was observed in between the NbC diffusion barrier and the Mo layer in this specimen. As noted in Section 3.0, there was considerable outgassing in the vacuum furnace during thermal cycling most likely due to inadvertent entrapped moisture in the specimen from the sectioning process. It is suggested that this reaction product was due to moisture attack and not due to reaction during CVD.

Figure 11(a) to (g) show the EDS from spot analyses of the different layers and the out-of-plane reaction product observed in DS-2 shown in Figure 10(a) and (b). Large C peaks observed in all the spectra could be due to two possible reasons. First, it is possible that these values are a genuine reflection of the C content in the coating layers due to a considerable amount of outward C diffusion from the Gr substrate during CVD. Second, the specimen surface could have been contaminated with C due to the decomposition of hydrocarbon contaminants present in the chamber during observations in the SEM [37,38,39]. As discussed in Section 4.4, it is suggested that the high values of C reported in this paper are attributed to hydrocarbon contamination of the specimen surface. Without a precise determination of the C content of these layers, the compositions of the coating layers shown in Figure 11(a) to (g) could not be unambiguously determined. Therefore, although the micrographs show the nominal compositions of the layers, it is cautioned that the actual compositions may be different.

Figure 11(a) shows the EDS from the Mo overlay in DS-2, where the strong Mo peak confirmed the presence of Mo. In contrast, there was no detectable O in this layer, which is consistent with the fact that the Mo overlay was well-bonded to the ZrC layer. Similarly, a strong Zr peak was observed from the ZrC region with no evidence of elemental diffusion from the other layers (Figure 11(b)). In the layer marked “Nb” in Figure 11(c), the EDS peaks showed strong evidence of Mo and Zr diffusion into the region from both the Mo layer below and the ZrC above it, respectively, during the CVD process. In contrast, the EDS peaks from the Mo layer deposited on the NbC diffusion barrier showed only the expected strong Mo peak with no other elements being detected thereby suggesting that neither Nb or Zr had diffused into this layer during the coating process (Figure 11(d)). Significantly, both the Mo overlay (Figure 11(a)) and the Mo internal layer (Figure 11(d)) did not reveal any detectable levels of O, which correlated well with the fact that both these Mo layers were well-bonded with the adjacent layers. An EDS spot analysis from the post-polishing reaction layer showed Mo, Nb, O peaks in addition to a very large C peak compared to the other layers (Figure 11(e)). Il’in et al. [40] attributed the formation of NbO_2 and Nb_2O_5 phases in a NbC/C composite to chemical attack by atmospheric oxygen and moisture during metallographic sample preparation. In the present instance, it appears that the environmental attack is attributed to moisture that was entrapped in the debonded Mo/NbC interface and inadequate drying after periodic specimen sectioning for metallography (Figure 10(a) to (b)). Since the EDS results from the NbC diffusion barrier revealed only a strong Nb peak and not an O peak (Figure 11(f) to (g)), it appears that the reaction product forms preferentially on the Mo layer rather than on the NbC layer of the Mo/NbC interface. Thus, the reaction product may be either a (Mo,Nb) oxide or (Mo,Nb)OH layer.

4.2 Microstructures of Thermally Cycled Specimens

The DS-2 specimen was thermally cycled in stepped heat-cool experiments from 1000 to 1900 K with 1 h hold time at each temperature, where metallographic samples were cut from the disk after each thermal cycle (Figure 12(a) to (l)). Thus, each metallographic sample had experienced an additional 1 h hold time at a temperature 100 K above that used in the previous thermal cycle (Figure 12(b) to (k)). The last remnant specimen was directly thermally cycled for an additional nine cycles at 1900 K (Figure 12(l)). Thus, the last remnant piece had experienced a total of 19 thermal cycles between 1000 and 1900 K including ten cycles only at 1900 K at the end of the test. As noted in Section 3.0, there was extensive outgassing in the vacuum furnace each time the specimen was re-introduced to conduct the next thermal cycle. This outgassing

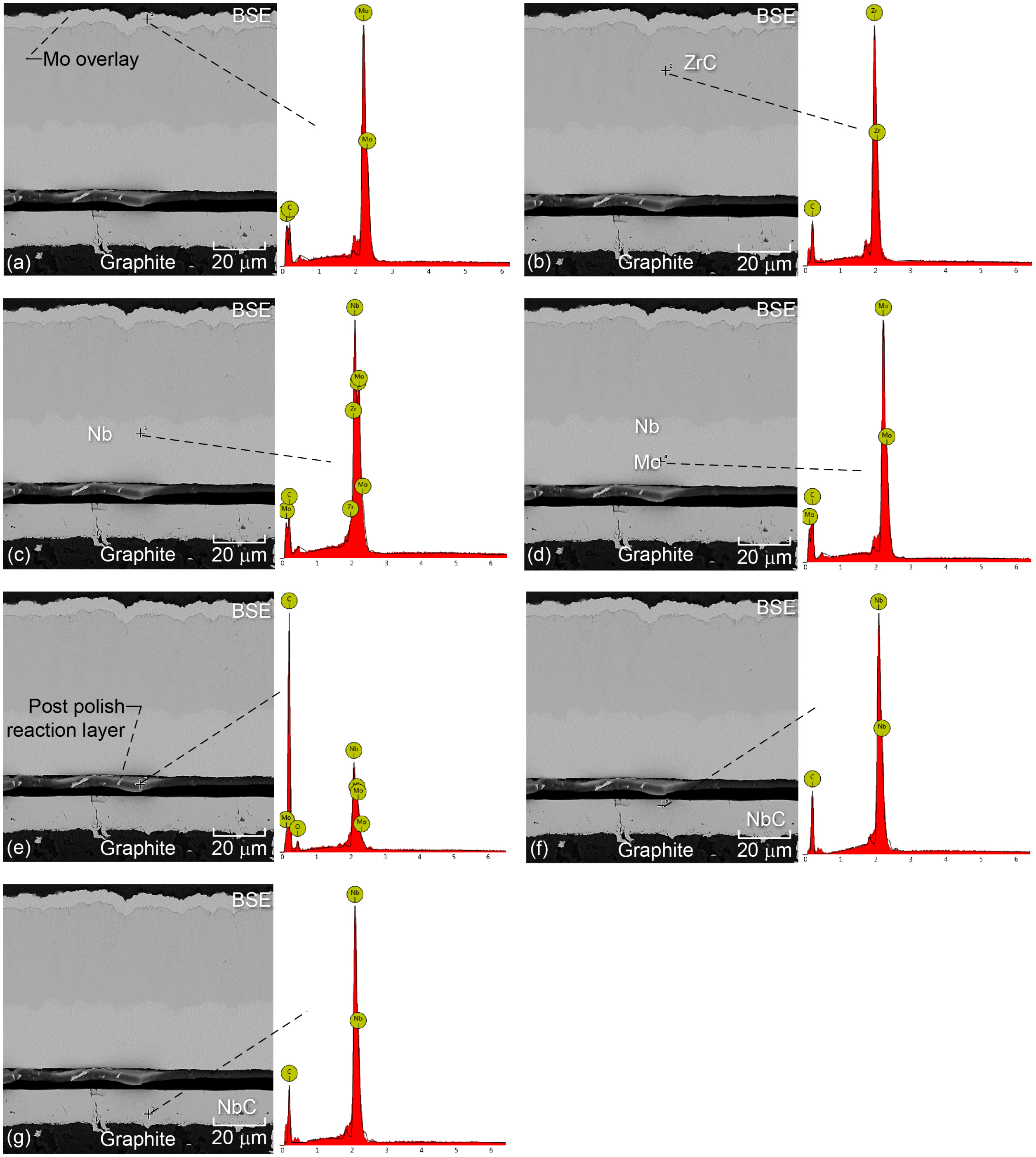

Figure 11.—(a) to (g) Back scattered electron images and corresponding EDS of the different layers in the as-coated disk specimen, DS-2. The measured high values of carbon are suspect as they could have been affected by hydrocarbon contamination in the SEM chamber.

was attributed to entrapped moisture and inadequate drying of the specimen after sectioning off pieces for metallographic observations. The as-received microstructures for DS-2 were described in Section 4.1 (Figure 10(a) to (b) and Figure 11(a) to (g)). Figure 13(a) to (f) show the progressive change in the microstructures of the coating layers after stepped thermal cycling from room temperature to 1900 K. After thermally cycling at 1000 and 1100 K, vertical cracks were observed in the ZrC in some regions (Figure 13(b)). A comparison of Figure 10(b) and Figure 13(b) suggest that these vertical cracks may have been present in the as-received coated specimen, and therefore, they may not have originated during thermal cycling. There appeared to be no significant change in the coating microstructures until 1700 K (Figure 13(c) to (e)). At and above 1700 K, the vertical cracks previously observed in the ZrC layer had now penetrated into the "Nb" layer. Although some cracks were observed in the NbC diffusion layer in the as-received microstructure (Figure 13(a)), thermal cycling at and above 1700 K resulted in several cracks in the NbC layer both horizontal and vertical to the NbC/Mo interface (Figure 13(e) to (f)). Additional nine thermal cycles at 1900 K resulted in some of the vertical cracks penetrating all the coating layers from the Mo overlay to the Gr substrate. Significantly, the Mo overlay did not debond and the cracks did not penetrate it.

Figure 14 shows a spot EDS elemental analyses for C, O, Mo, Nb and Zr of these thermally cycled coated layers. A close examination of these data revealed that there was a relatively small amount of Zr diffusion from the ZrC into the adjacent Mo overlay and the Nb layers. In this case, the Zr content was measured to be less than 5 at.%. There was no corresponding significant diffusion of Mo and Nb into the ZrC. There was also significant Mo diffusion into the Nb layer sandwiched between the ZrC and Mo layer, where the Mo content was less than 10 at.%. There was no significant diffusion of Nb and Zr into the Mo layer adjacent to the NbC diffusion barrier. Once again, the observed C content was high varying between about 35 and 40 at.% most of which are attributed to hydrocarbon contamination as discussed earlier. The relatively high O levels varying between 15 and 20 at.% in all the layers appear to have been picked up during thermal cycling since the as-received microstructures did not show detectable amount of O (Figure 11(a) to (d), (f) and (g))). As noted in Section 3.0, there was probably entrapped moisture in the specimen after each stage of sectioning, which appears to be the source of this O contamination of the vacuum furnace.

Specimen DS-1 corresponding to the as-received microstructures shown in Figure 9(a) to (d) was continuously thermally cycled between ambient temperature and 1900 K for 20 cycles with a 1 h hold time at 1900 K. The post-cycling microstructures at different locations within the specimen revealed a considerable amount of void formation in the ZrC layer and damage accumulation in several regions of the Nb/ZrC interface leading to localized debonding at the interface (Figure 15(a) and (b)). These pores in the ZrC layer appeared to be Kirkendall porosity likely caused by preferential diffusion of Zr from the ZrC layer towards the Nb layer. Through thickness cracks were observed in some areas progressing through all the layers from ZrC to the Gr substrate (Figure 15(b)).

Figure 16(a) shows the post-thermal cycling spot EDS spectra and compositions determined at the red dots from the different coating layers for DS-1. Again, a high level of C varying between 32 and 39 at.% was observed in all the layers. A close examination of the data shows that Zr had preferentially diffused from the ZrC layer into the Nb and the Mo layers below. In this case, the Zr content varied from about 60.8 at.% in ZrC to 5.5 at.% in Nb to 2.1-3.1 at.% in Mo. The Nb-Zr binary phase diagram shows that the β-Nb and β-Zr phases[6] are completely isomorphous at high temperatures and undergo a monotectoid reaction at and below 893 K to form a β-Nb + α-Zr dual phase microstructure [41]. The higher solid solubility of Zr in Nb and the lower solid solubility of Nb in Zr may qualitatively explain why Zr had preferentially diffused from the ZrC into the Nb layer during the thermal cycling test.

---

[6] α and β represent the hcp and bcc crystal structures, respectively.

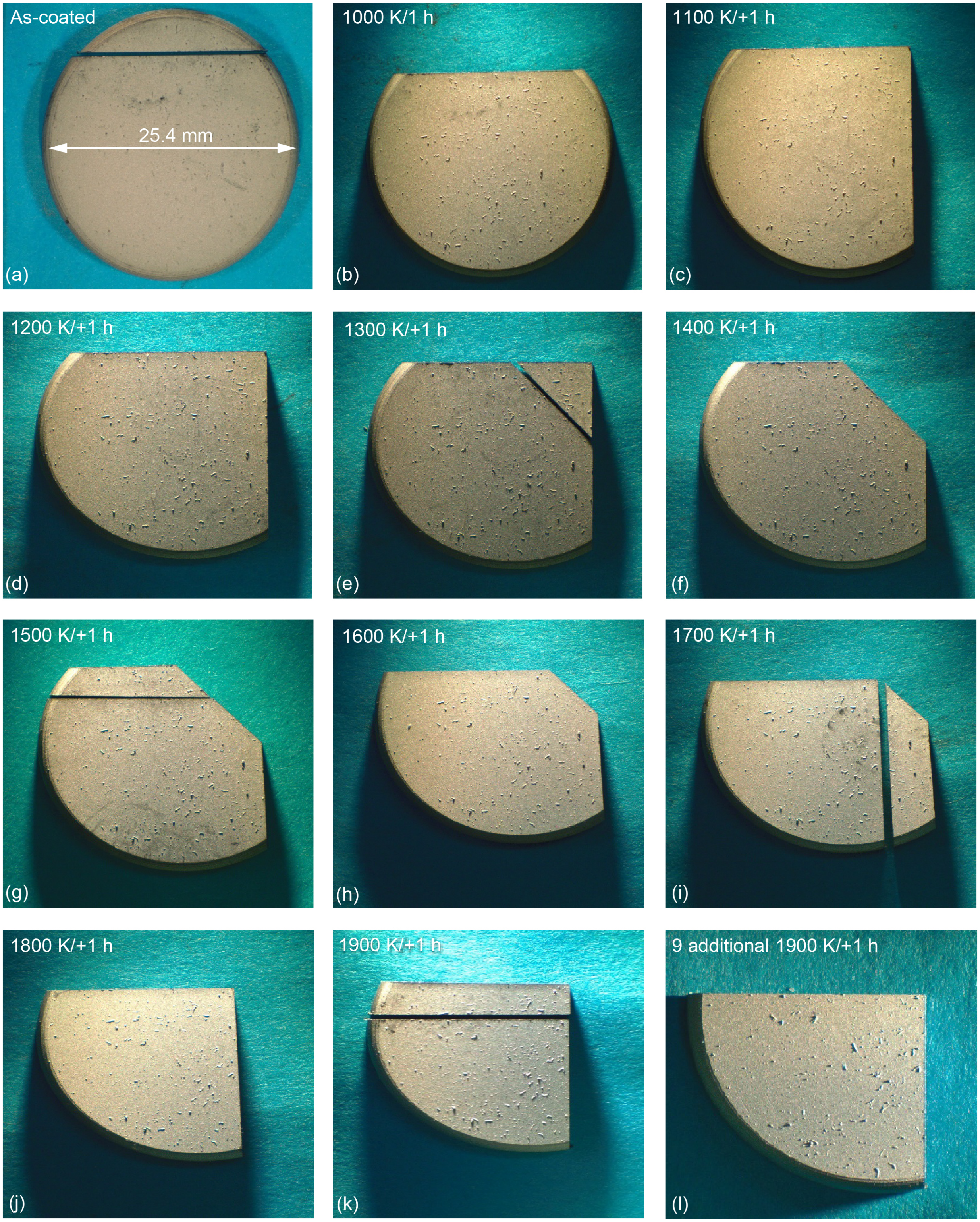

Figure 12.—(a) to (l) Optical macrographs of the as-received and sectioned DS-2 after each stepped heat-cool thermal cycle.

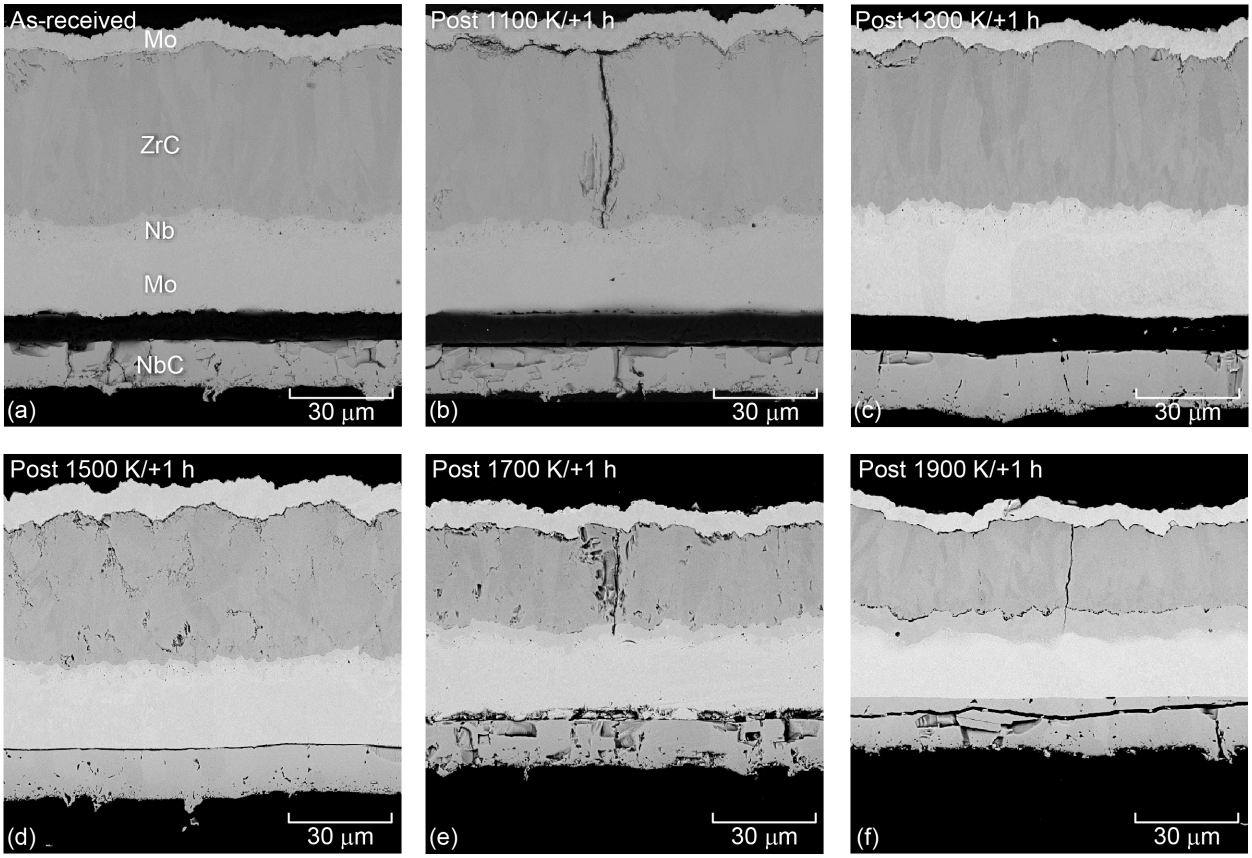

Figure 13.—Back scattered electron images of the cross-sectional microstructures after step thermal cycling specimen, DS-2, at temperatures between 1000 and 1900 K with 1 h hold times at temperature. (a) As-received; (b) 1100 K; (c) 1300 K; (d) 1500 K; (e) 1700 K; and (f) 1900 K.

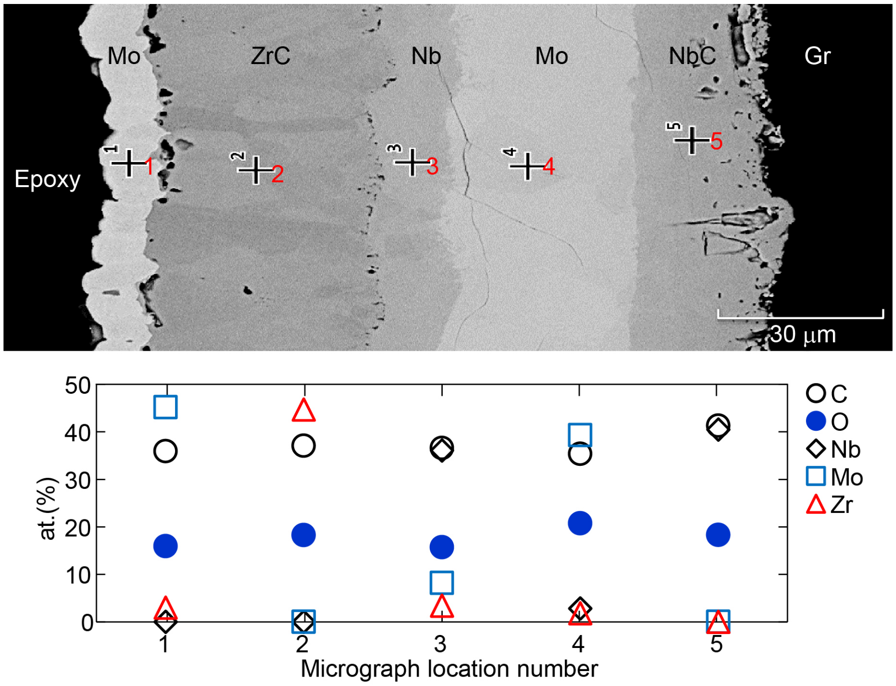

Figure 14.—Back scattered electron image of a region of the post-step thermal cycled specimen, DS-2, showing the locations in each coating layer at which the spot EDS data shown in the bottom graph were determined. The measured values of carbon are suspect as they could have been affected by hydrocarbon contamination in the SEM chamber. The source of oxygen appears to be due to moisture contamination of the vacuum furnace due to inadequate drying of the specimen prior to thermal cycling.

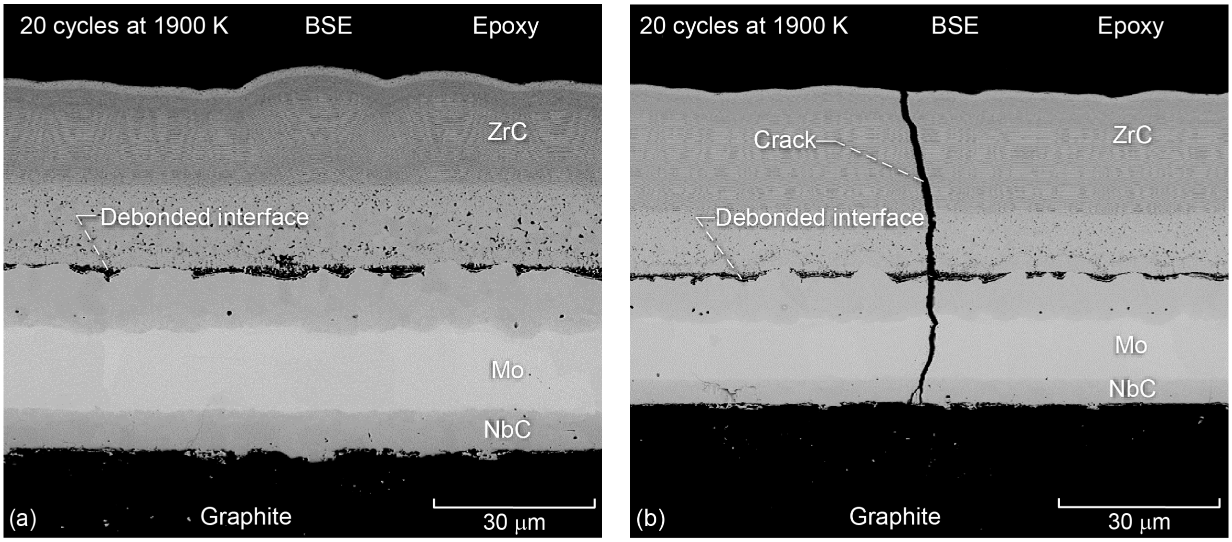

Figure 15.—Back scattered electron images of two different regions of the specimen, DS-1, after thermally cycling between ambient and 1900 K with a 1 h hold time for 20 cycles. (a) Large amounts of voids were observed in the ZrC layer. (b) Transverse cracks observed in the ZrC layer in the as-received specimen had propagated to the Gr substrate.

The compositions of the two spots in the Mo layer also revealed that Nb had diffused into this layer. Significantly, the compositions of O varied between 14.0 to 19.6 at.% close to the Nb and NbC diffusion layers, respectively. A spot EDS analysis of the Mo overlay also revealed a high O level of 22.9 at.% (Figure 16(b)). A high O level of 20.8 at.% was also observed in the NbC diffusion layer. Since the ZrC and the Nb layers did not contain significant amounts of O in the post-thermal cycled specimen, it is reasonable to conclude that the high levels of O observed in the Mo overlay, the Mo and the NbC layers were due to oxygen contamination of the CVD reactor chamber during the coating process. The fact that O peaks were not observed in the ZrC and the Nb layers suggests the possibility that the oxygen contamination is intimately connected with the deposition of Mo. Infrared spectral analyses of vaporized $MoCl_5$ salt at elevated temperatures revealed the presence of oxygen impurity in the form of $MoOCl_3$ [42]. It is likely that the source of the oxygen contamination was the CVD precursor $MoCl_5$ salt although the possibility of a leak in CVD system cannot be ruled out. The source of the O in the NbC layer is most likely from $NbOCl_3$ impurity present in the precursor $NbCl_5$ salt assuming that there was no air leakage in the CVD system [43]. As will be demonstrated later in the paper, high values of oxygen were observed quite often in the Mo layers. Similarly, high values of O were observed in the Mo layer in an earlier investigation [25].

Figure 16(c) shows the variations in the C and Zr compositions at seven locations in the ZrC layer varying from the Mo overlay/ZrC to the ZrC/Nb interfaces after thermal cycling. The compositional data are shown both in a graphical as well as in a tabular form. The observed C and Zr compositions varied between 36.9 and 46.8 at.%, and 53.2 and 63.2 at.%, respectively. There was no significant spatial variation in the compositions of these two elements. Unfortunately, as mentioned earlier, the observed C values were probably influenced by hydrocarbon contamination on the specimen surface so that the true C value is unknown. As noted earlier, the ZrC layers were probably deposited under CVD processing which resulted in a two-phase lamellar microstructure corresponding to either the ZrC + C + gas or the ZrC + Zr + gas regions of the CVD pseudo-binary phase diagrams [36]. On the basis of the Zr-C binary phase diagram [29], the expected microstructure for $C < 38.0$ at.% would be an α-Zr + ZrC lamellar eutectic microstructure at room temperature. Between $38.0 \leq C \leq 46.5$ at.%, the microstructure is expected to be a single phase Zr-rich ZrC_x microstructure. Referring to Figure 16(c), the average measured value of C is about 41.5 at.%. It is reasonable to assume that the actual average value of C would be less than 38.0 at.% after correcting for contributions from C deposits from hydrocarbon decomposition. This assumption is consistent with the observed lamellar eutectic microstructure (Figure 9(b) to (c) and Figure 16(c)) based on the Zr-C binary phase diagram [29] and the CVD pseudo-binary phase diagram [36].

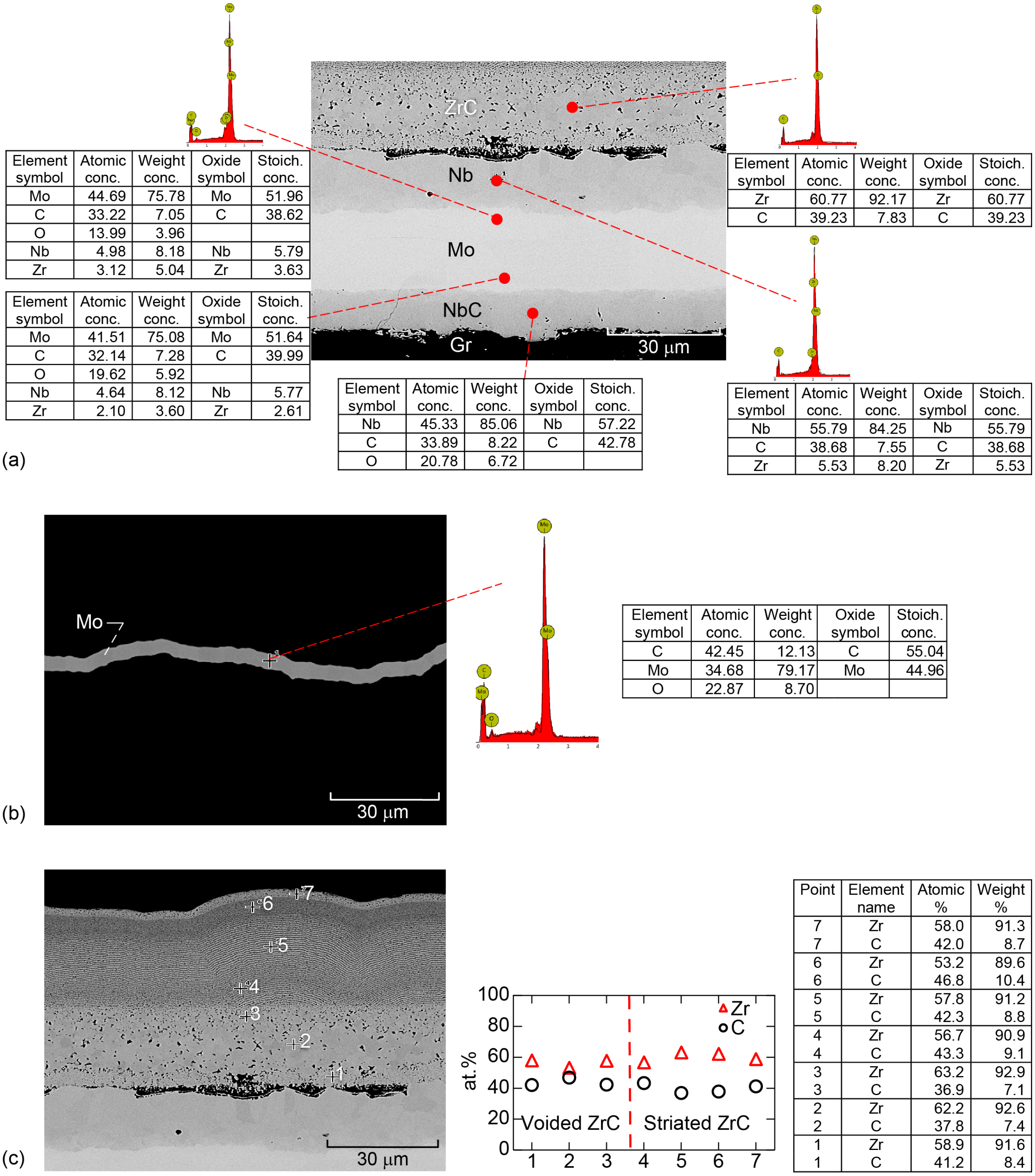

Element symbol	Atomic conc.	Weight conc.	Oxide symbol	Stoich. conc.
Mo	44.69	75.78	Mo	51.96
C	33.22	7.05	C	38.62
O	13.99	3.96		
Nb	4.98	8.18	Nb	5.79
Zr	3.12	5.04	Zr	3.63

Element symbol	Atomic conc.	Weight conc.	Oxide symbol	Stoich. conc.
Mo	41.51	75.08	Mo	51.64
C	32.14	7.28	C	39.99
O	19.62	5.92		
Nb	4.64	8.12	Nb	5.77
Zr	2.10	3.60	Zr	2.61

Element symbol	Atomic conc.	Weight conc.	Oxide symbol	Stoich. conc.
Nb	45.33	85.06	Nb	57.22
C	33.89	8.22	C	42.78
O	20.78	6.72		

Element symbol	Atomic conc.	Weight conc.	Oxide symbol	Stoich. conc.
Zr	60.77	92.17	Zr	60.77
C	39.23	7.83	C	39.23

Element symbol	Atomic conc.	Weight conc.	Oxide symbol	Stoich. conc.
Nb	55.79	84.25	Nb	55.79
C	38.68	7.55	C	38.68
Zr	5.53	8.20	Zr	5.53

Element symbol	Atomic conc.	Weight conc.	Oxide symbol	Stoich. conc.
C	42.45	12.13	C	55.04
Mo	34.68	79.17	Mo	44.96
O	22.87	8.70		

Point	Element name	Atomic %	Weight %
7	Zr	58.0	91.3
7	C	42.0	8.7
6	Zr	53.2	89.6
6	C	46.8	10.4
5	Zr	57.8	91.2
5	C	42.3	8.8
4	Zr	56.7	90.9
4	C	43.3	9.1
3	Zr	63.2	92.9
3	C	36.9	7.1
2	Zr	62.2	92.6
2	C	37.8	7.4
1	Zr	58.9	91.6
1	C	41.2	8.4

Figure 16.—Spot EDS data from the different coating layers in specimen, DS-1, after thermal cycling between ambient and 1900 K with a 1 h hold time for 20 cycles. The measured values of carbon are suspect as they could have been affected by hydrocarbon contamination in the SEM chamber. (a) General analysis of the different layers showing high values of oxygen in the Mo and the NbC layers as well as evidence of Zr diffusion into the Nb and the Mo layers. (b) High values of oxygen in the debonded Mo overlay layer. (c) Variations of C and Zr at seven locations in the ZrC layer from close to the Nb/ZrC interface to the ZrC/Mo overlay interface showing no significant spatial variations in the compositions of these two elements.

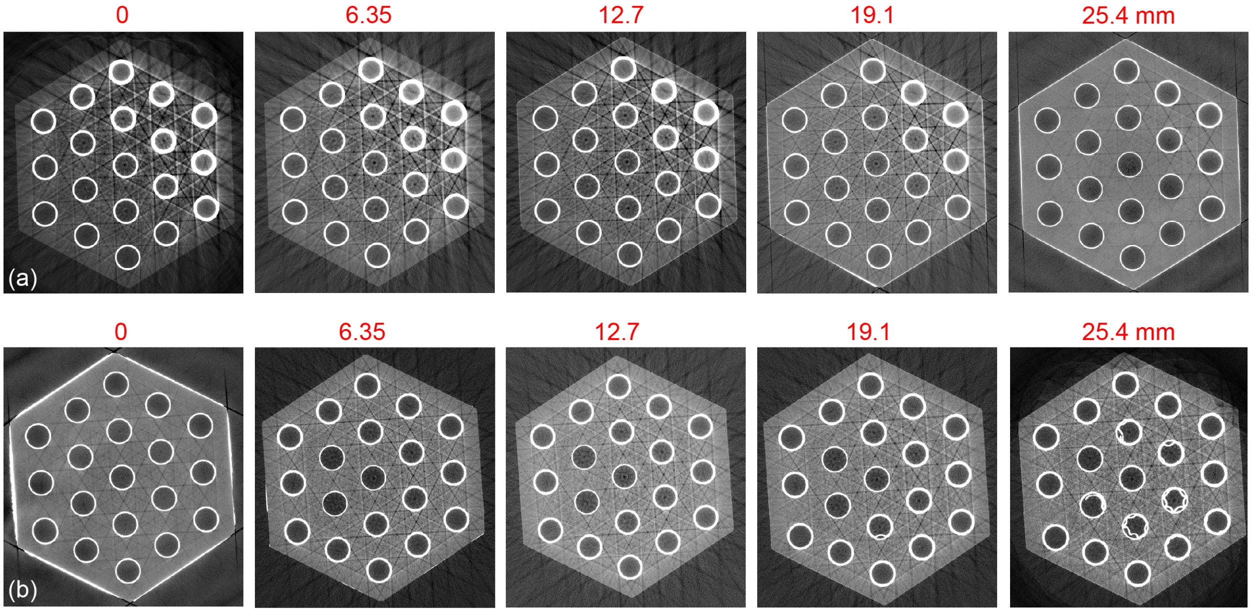

Figure 17.—Micro-CT scanned images of 25.4 mm length from end faces A and B of the coated graphite specimen shown in Figure 6 demonstrating that all the 19 channels were coated.

4.3 Micro-CT Scan of the Hexagonal Rod

Figure 17(a) and (b) show the CT scan images of the multilayered coated hexagonal rod scanned from ends A and B, respectively (Figure 6). Although an image was generated at every 10 µm voxel interval thereby generating a total of ~2800 images, Figure 17(a) and (b) only show the images obtained at 0, 6.35, 12.7, 19.1 and 25.4 mm locations from the end faces. The vendor did not specifically identify the end face which corresponded to the gas inlet end. For the images obtained from end face, A, the coating thicknesses within the channels decrease with increasing depth from 0 to 25.4 mm (Figure 17(a)). Moreover, the coatings were thicker in channels approximately located in the first quadrant to the right of the center channel. These observations suggest that either the gas mass flow rates and/or the temperature distribution in these channels were probably higher than in the other neighboring channels. Additionally, lower gas back pressure in a channel compared to its neighbor would ensure a higher gas flow rate due to the law of least resistance. There was no evidence of coating debonding in these images but the resolutions of the CT scanned images were insufficient to resolve the different layers presumably because the atomic numbers of Mo (42), Nb (41) and Zr (40) are close [44]. It is important to note that the differences in the densities of Mo, Nb and Zr, which are 10.2, 8.57 and 6.49 g/cc, respectively, are too large to account for this poor resolution [45]. The CT scanned images from end face, B, revealed that all the channels were coated. Some debonding was observed in a few channels in the two images obtained at 19.1 and 25.4 mm from the end (Figure 17(b)).

4.4 Transverse Microstructures of the Coated Channels in the Hexagonal Rod

Figure 18(a) to (g) show optical macrographs of the transverse coated sections 1T to 7T. In comparison to the CT scanned images (Figure 17(a) and (b)), where all the channels appeared to be coated, the coatings in several locations with the some channels were not distinctly visible either because they were missing or they were too thin to be resolved at the low magnifications. Detailed low magnification SEM images confirmed that all the channels were coated along the length of the rod. Figure 19(a) to (c) show examples of three coated and equally-spaced channels 4T-1-2, 4T-3-3 and 4T-5-2 in section 4T, where the coating

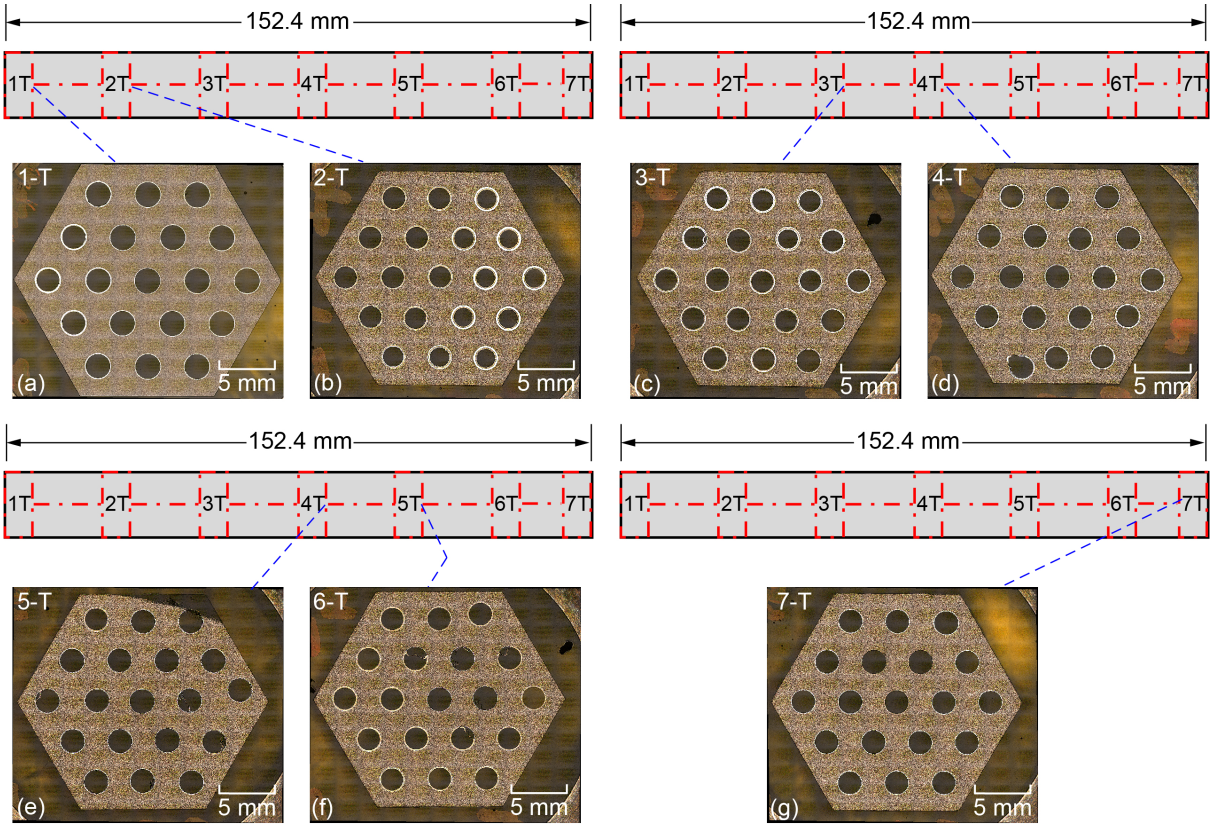

Figure 18.—(a) to (g) Optical macrographs of the seven transverse sections of the 152.4 mm long coated hexagonal rod shown in Figure 6.

layers in channels 4T-1-2 and 4T-5-2 appeared to be debonded. High magnification SE images revealed that the Mo overlay layer had either debonded from the ZrC layer or it was completely absent (Figure 20(a), Figure 21(a) and Figure 22(a)).

Figure 20(a), Figure 21(a) and Figure 22(a) show the SE images and the corresponding x-ray elemental maps for C, O, Cl, Nb, Mo and Zr from randomly chosen sections of the multilayered coatings in the channels 4T-1-2, 4T-3-3 and 4T-5-2, respectively[7]. It is important to note that the legend identifying each layer in the SE images is based on nominal compositions and that the actual compositions may be significantly different. The bright C maps correspond to the Gr substrate, cracks, debonded regions and porosity, and the epoxy mount. In contrast, they are barely visible in the other regions of the SE images. Significantly, the O maps correspond closely to the Mo and Mo overlay layers of the coating thereby confirming the earlier observations on the coated disk specimens (Section 4.1 and 4.2). Once again, the Mo overlay layers were observed to have debonded from the ZrC layers in the microstructures. Also, a high concentration of O in the Mo close to the NbC/Mo appears to have resulted in the debonding of this interface (Figure 21(a)). Thus, elimination of O from the CVD reactor is critical to ensuring good bonding between the adjacent layers. Interestingly, the Cl maps, although weak in intensity, are aligned with the Mo and O maps. Vapor deposition investigations of NbC and ZrC coatings by thermal decomposition of Nb and Zr halogen salts, respectively, revealed that the Cl and the O impurity levels decreased nonlinearly with increasing coating temperature [8,9]. In this case, the Cl was about 1.0 at 1423 K and decreased to 0 wt.% above 1573 K

---

[7] It is noted that the order of the elemental x-ray maps are organized to correlate with the order of the coating layers from the Gr substrate to the Mo overlay.

during the deposition of the ZrC coating using $ZrCl_4$. Correspondingly, the O decreased from over 2 wt.% at 1373 K to 0 wt.% above 1623 K. As discussed earlier, the source of the O is most likely from the $MoOCl_3$ impurity present in the $MoCl_5$ precursor salt [42]. Thus, observation of a weak Cl and O EDS maps in conjunction with that for the Mo layer is consistent with the $MoOCl_3$ impurity as the source of both these impurities. It is likely that increasing the deposition temperature for Mo would eliminate these impurities.

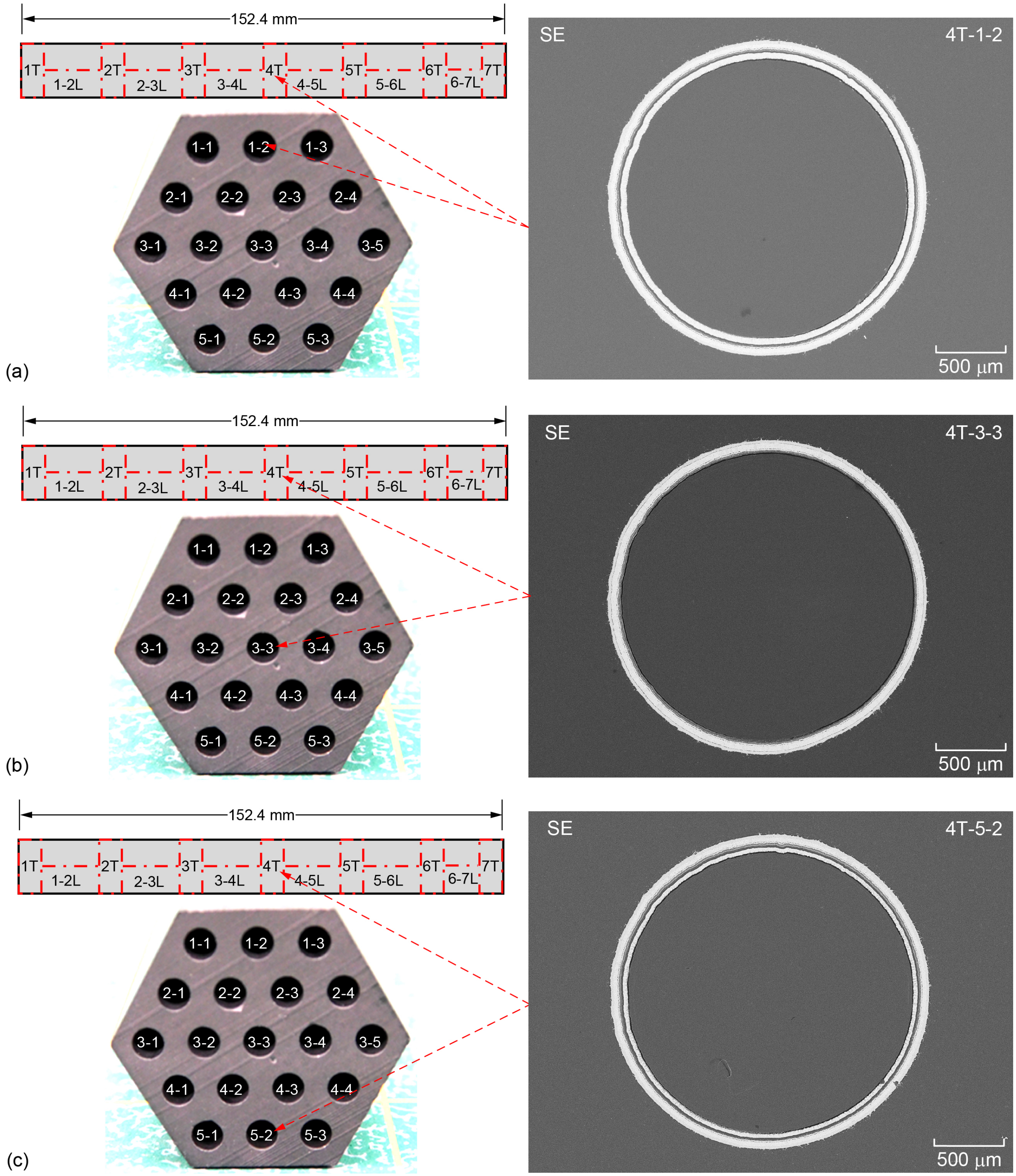

Figure 19.—Secondary electron images of channels (a) 4T-1-2, (b) 4T-3-3 and (c) 4T-5-2 in the transverse section 4T of the 152.4 mm long coated hexagonal rod shown in Figure 6.

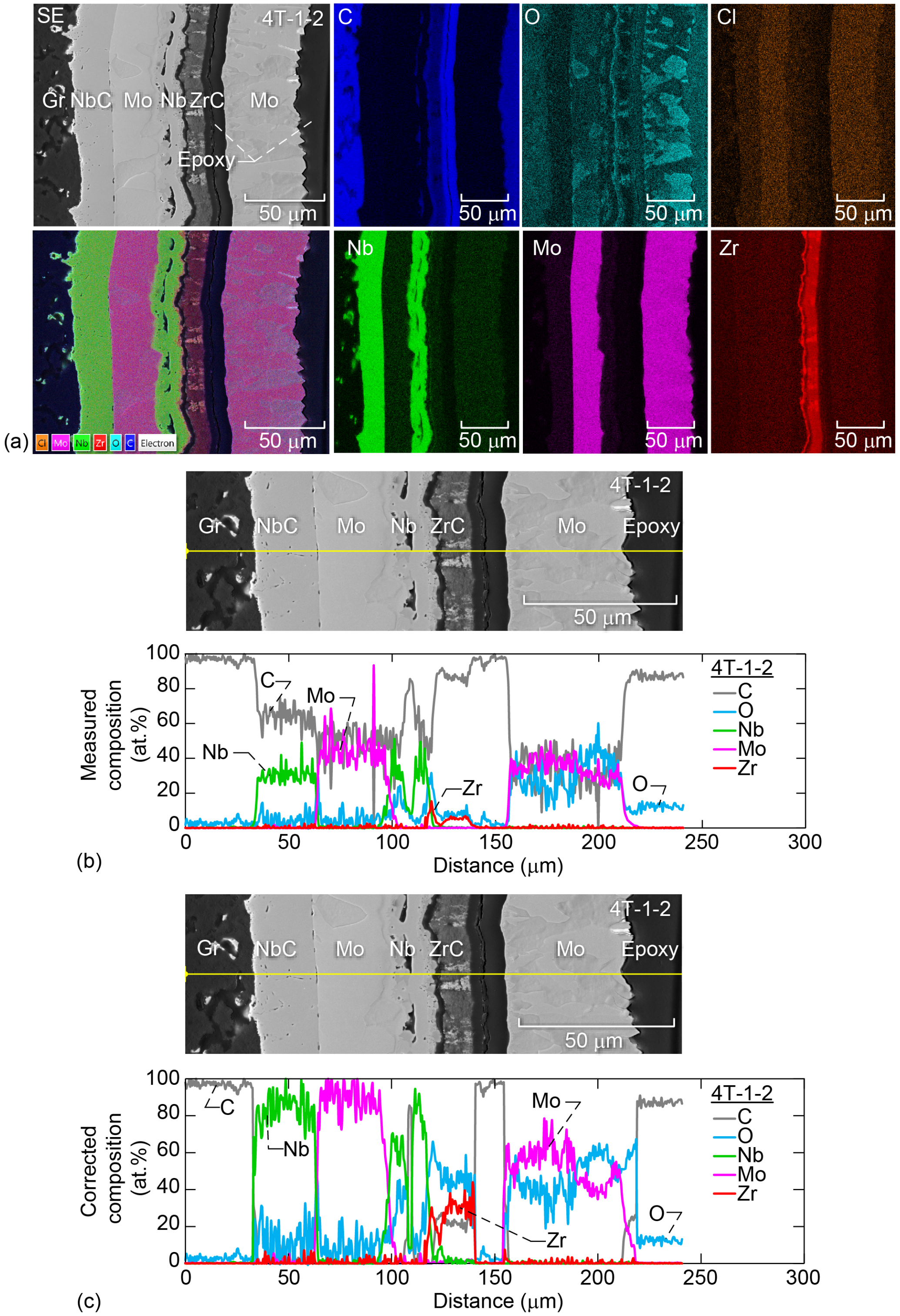

Figure 20.—(a) Secondary electron image and corresponding EDS maps for C, O, Cl, Nb, Mo and Zr for channel 4T-1-2. (b) Experimental line scan compositional profiles for C, O, Nb, Mo and Zr along the yellow line for the micrograph shown in (a). (c) Corrected line scan compositional profiles for C, O, Nb, Mo and Zr of the data shown in (b).

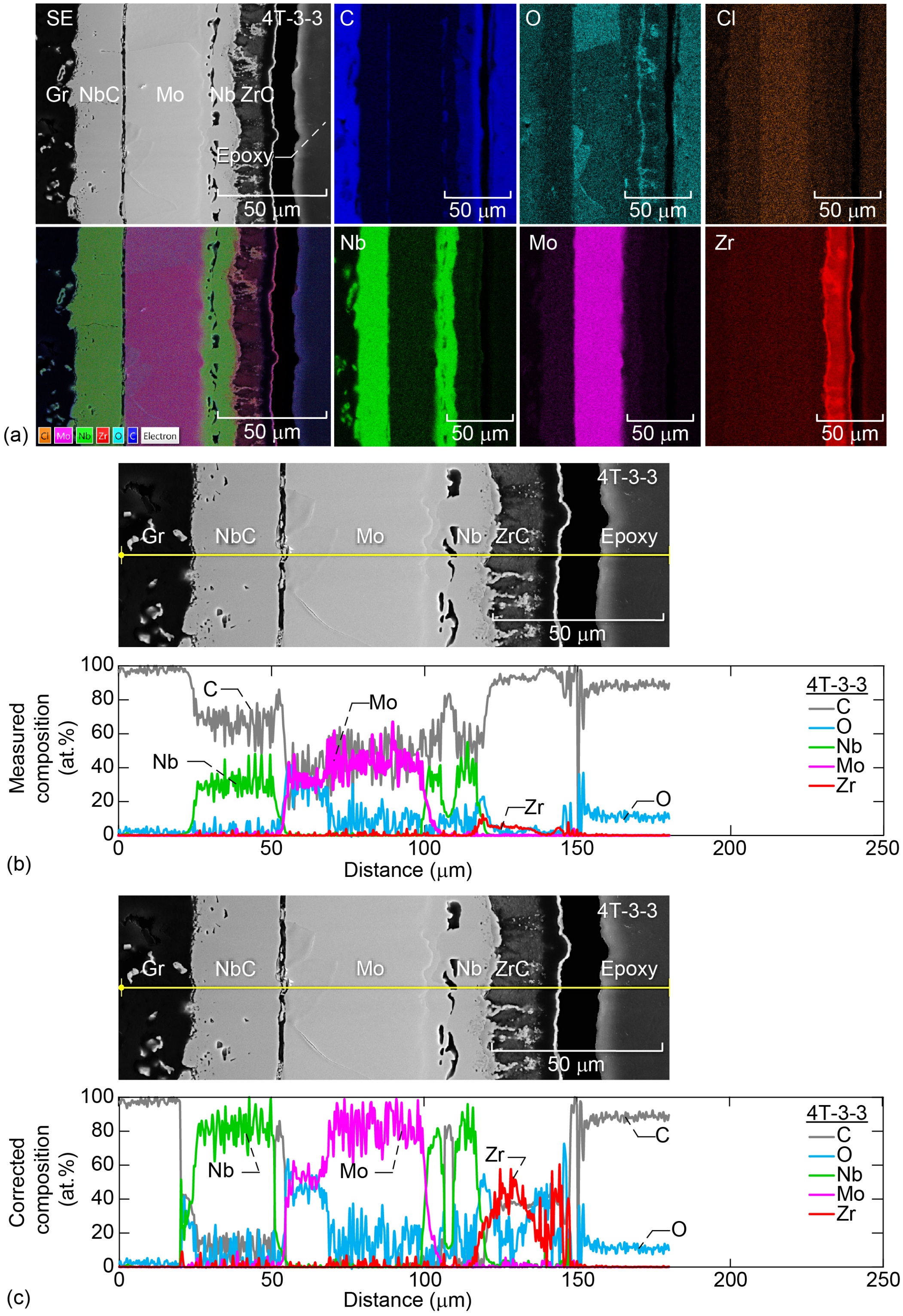

Figure 21.—(a) Secondary electron image and corresponding EDS maps for C, O, Cl, Nb, Mo and Zr for channel 4T-3-3. (b) Experimental line scan compositional profiles for C, O, Nb, Mo and Zr along the yellow line for the micrograph shown in (a). (c) Corrected line scan compositional profiles for C, O, Nb, Mo and Zr of the data shown in (b).

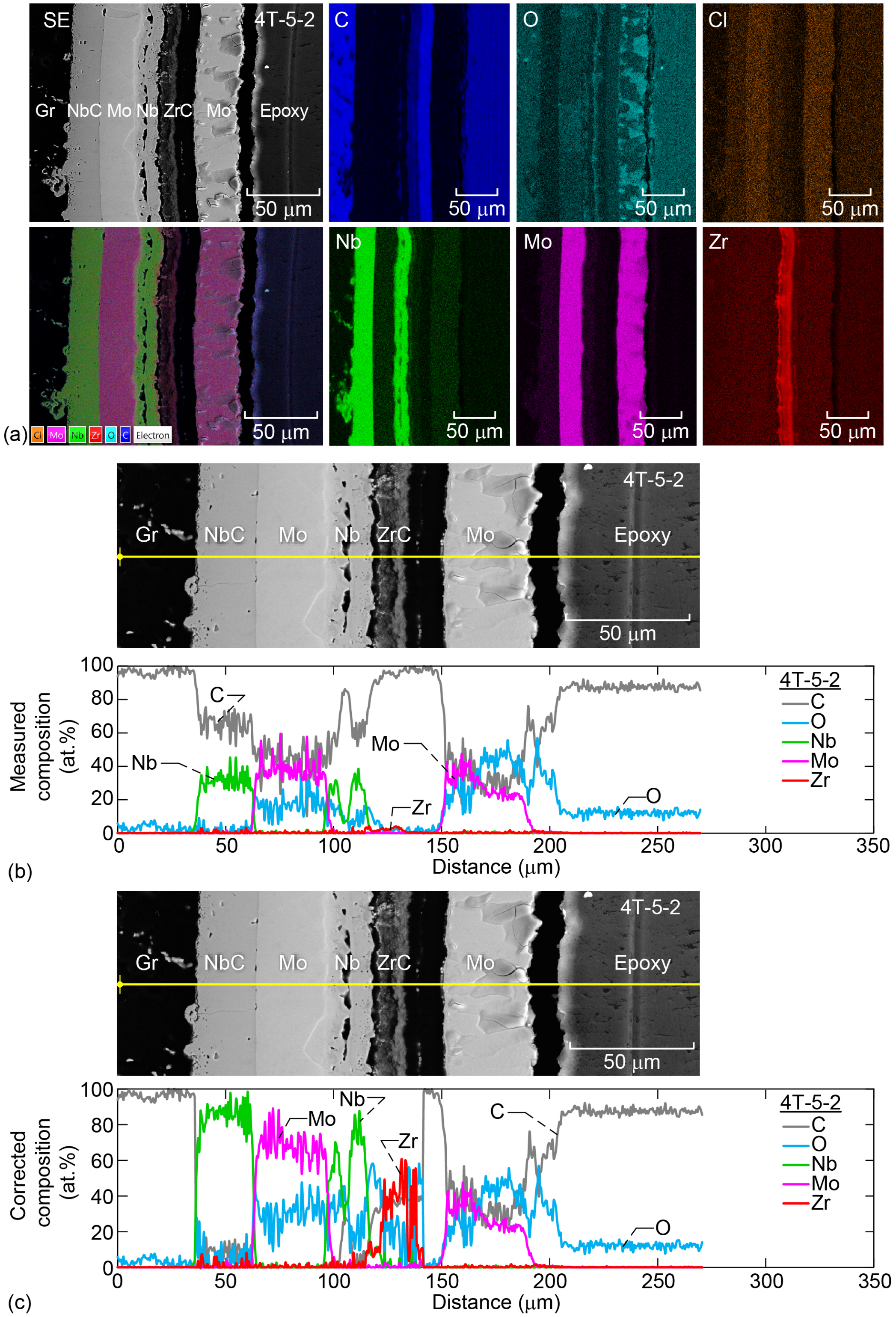

Figure 22.—(a) Secondary electron image and corresponding EDS maps for C, O, Cl, Nb, Mo and Zr for channel 4T-5-2. (b) Experimental line scan compositional profiles for C, O, Nb, Mo and Zr along the yellow line for the micrograph shown in (a). (c) Corrected line scan compositional profiles for C, O, Nb, Mo and Zr of the data shown in (b).

Figure 20(b), Figure 21(b) and Figure 22(b) show the corresponding experimental line scans for these elements except Cl for which the amounts were largely close to 0 at.%. The amounts of C observed in the coatings were once again very high in the line scans but hardly visible in the EDS maps including for the NbC and ZrC layers. The amount of C detected in these coatings was lower than those observed in the second disk specimen (Figure 11(a) to (g)). The specimens were re-coated with Pt without removing the earlier Pt layer to minimize specimen charging, and subsequently plasma cleansed within the SEM for 300, 600 and 1200 s in order to reduce surface C deposits. A comparison of the line scan results before and after plasma cleansing did not show any significant change in the C composition even after plasma cleansing for 1200 s. As noted earlier, the reason for these high values of C could be due to either diffusion from the Gr substrate during the CVD process or due to hydrocarbon contaminants on the specimen surface [37,38,39]. An examination of the Nb-C binary phase diagram reveals that the expected equilibrium phases are NbC_{1-x} + C when C > 50 at.% [46]. In this case, it is expected that the morphology of the two-phase microstructure would consist of either alternating NbC/C lamellar plates or a dispersion of NbC spheroids in a Gr matrix depending on the highest temperature reached by this layer during the CVD process. Since the experimentally measured values of C in the NbC layer exceeds 60 at.% (Figure 20(b), Figure 21(b) and Figure 22(b)), it is expected that this layer should consist of an eutectic two-phase NbC_{1-x} + C microstructure. However, a careful microstructural examination of the NbC layer at high magnifications in specimen 4T-5-2 revealed a single phase microstructure (Figure 23(a) to (d)). Even the Mo, Nb, ZrC and the Mo overlay layers were single phase microstructures. Thus, it is reasonable to assume that the high values of C reported in this paper are most likely due to C deposits from hydrocarbon contaminants on the specimen surface[8].

In order to correct for this excess carbon due to surface contamination, it appears reasonable to assume that the Nb layer sandwiched between the Mo and the ZrC layers does not contain significant amounts of carbon assuming that C diffusion from the Gr substrate was negligible during CVD. After carefully matching the measured compositional line scans with the SE images, an average value of the C measured in the Nb layer, $(C_{avg})_{Nb}$ was evaluated and subtracted out from the measured values of C for the other layers, $(C_{measured})_x$, where x is the nominal composition of the layer. Thus,

$$(C_{correct})_x = (C_{measured})_x - (C_{avg})_{Nb} \tag{5}$$

where $(C_{correct})_x$ is the corrected value of C in layer x. The correction factor, CF, is then given by[9]

$$CF = \frac{[100-(C_{correct})_x]}{[100-(C_{measured})_x]} \tag{6}$$

The measured values of Mo, Nb, Zr, Cl and O were multiplied by CF to arrive at the corrected values for each element.

Figure 20(c), Figure 21(c) and Figure 22(c) show the corrected values of the compositional line scans for 4T-1-2, 4T-3-3, and 4T-5-2, respectively. The C line scans are consistent with the EDS maps (Figure 20(a), Figure 21(a) and Figure 22(a)). Table I tabulates the corrected values of C for the NbC layers in the three channels. As expected, there was a C gradient from the Gr substrate to the Mo coating layer so that a diversity of equilibrium phases are expected based on the Nb-C binary phase diagram [46].

---

[8] It is important to note that if the true C levels were as high as 60 at.%, it is expected that the microstructures would be much darker than observed (Figure 23(a) to (d)).

[9] It is noted that the CF resulted in the sum of the corrected values for all the elements added to 100 at.%.

For the peripheral channels 4T-1-2 and 4T-5-2, the C values in the nominal NbC layer are lower than 32.5 at.% corresponding to the two-phase eutectic Nb + β-Nb_2C region of the Nb-C binary phase diagram [46]. In the case of the center channel, 4T-3-3, the corrected values of C are less than 43.5 at.% corresponding to a multi-phase microstructure consisting of a single phase short range ordered (SRO) Nb-rich NbC or long range ordered (LRO) Nb_6C_5 microstructure for C > 40 at.% to a duplex microstructure of Nb + β-Nb_2C for C <32.5 at.% [46,47]. As noted earlier, the NbC layer in specimen 4T-5-2 was observed to be single phase (Figure 23(a) to (d)). The average corrected value of C of this layer was about 1.8 wt.% (8 at.%) (Figure 22(c)). This low amount of C suggests that this layer is mostly unreacted single phase Nb, which would be consistent with the single phase microstructure Figure 22(c). The amount of C was predicted to be low in the Mo layer but higher in the ZrC layer consistent with the formation of either Zr-rich ZrC or α-Zr + ZrC depending on the C content [48].

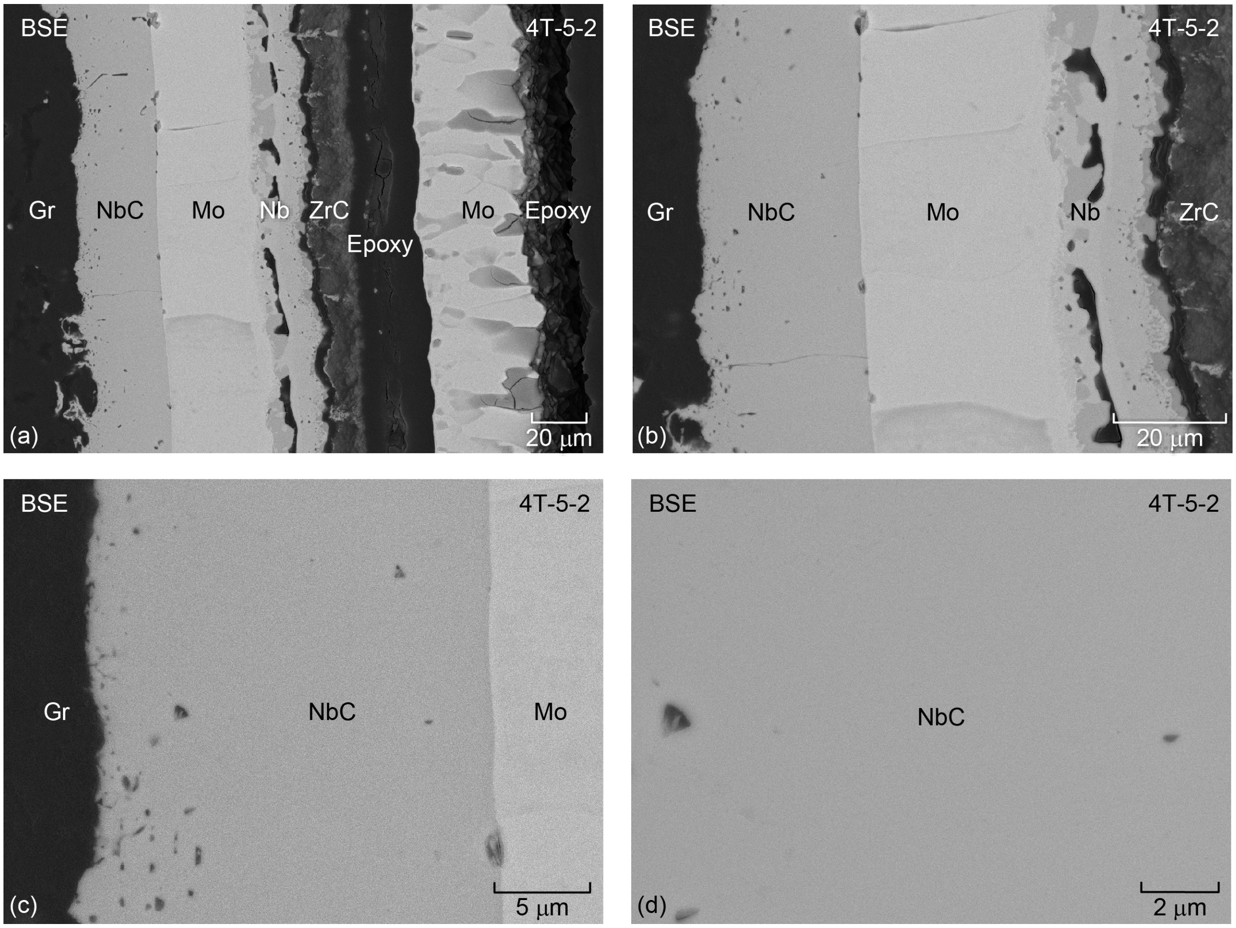

Figure 23.—(a) to (d) High magnification views of the coating layers in 4T-5-2 showing that all the layers are single phase.

TABLE I.—CORRECTED VALUES OF C FROM THE LINE SCANS OF CHANNELS 4T-1-2, 4T-3-3 AND 4T-5-2 AND THE PREDICTED MICROSTRUCTURES IN THE NBC LAYER BASED ON THE NB-C BINARY ALLOY PHASE DIAGRAM [46]

4T-1-2		4T-3-3		4T-5-2	
C (at.%)	Predicted phases	C (at.%)	Predicted phases	C (at.%)	Predicted phases
23.35	$Nb+Nb_2C$	45.32	NbC	30.01	$Nb+Nb_2C$
9.7	$Nb+Nb_2C$	44.43	NbC	26.94	$Nb+Nb_2C$
5.95	$Nb+Nb_2C$	44.36	NbC	17.63	$Nb+Nb_2C$
4.62	$Nb+Nb_2C$	42.41	NbC	9.36	$Nb+Nb_2C$
2.98	Nb	44.29	NbC	11.85	$Nb+Nb_2C$
2.95	Nb	42.72	NbC	0.5	$Nb+Nb_2C$
2.87	Nb	42.38	NbC	6.28	$Nb+Nb_2C$
2.76	Nb	41.86	NbC	3.52	$Nb+Nb_2C$
2.29	Nb	40.46	NbC	14.31	$Nb+Nb_2C$
2.1	Nb	38.97	$NbC+Nb_4C_{3-x}$	16.46	$Nb+Nb_2C$
2.94	Nb	35.3	$NbC+Nb_4C_{3-x}$	0	$Nb+Nb_2C$
2.94	Nb	32.74	$Nb+Nb_2C$	9.16	$Nb+Nb_2C$
3.23	Nb	32.57	$Nb+Nb_2C$	10.99	$Nb+Nb_2C$
2.88	Nb	16.76	$Nb+Nb_2C$	11.31	$Nb+Nb_2C$
2.5	Nb	26.5	$Nb+Nb_2C$	9.51	$Nb+Nb_2C$
2.79	Nb	20.97	$Nb+Nb_2C$	9.68	$Nb+Nb_2C$
2.8	Nb	11.19	$Nb+Nb_2C$	11	$Nb+Nb_2C$
3.1	Nb	17.32	$Nb+Nb_2C$	3.22	$Nb+Nb_2C$
2.94	Nb	15.33	$Nb+Nb_2C$	5.26	$Nb+Nb_2C$
3.05	Nb	15.73	$Nb+Nb_2C$	6.33	$Nb+Nb_2C$
2.76	Nb	19.08	$Nb+Nb_2C$	1.51	$Nb+Nb_2C$
2.92	Nb	15.91	$Nb+Nb_2C$	9.56	$Nb+Nb_2C$
2.32	Nb	11.44	$Nb+Nb_2C$	0	$Nb+Nb_2C$
2.59	Nb	14.22	$Nb+Nb_2C$	8.66	$Nb+Nb_2C$
2.93	Nb	11.01	$Nb+Nb_2C$	4.77	$Nb+Nb_2C$
2.79	Nb	16.6	$Nb+Nb_2C$	14.46	$Nb+Nb_2C$
2.76	Nb	21.41	$Nb+Nb_2C$	8.83	$Nb+Nb_2C$
3.54	Nb	11.67	$Nb+Nb_2C$	11.13	$Nb+Nb_2C$
2.17	Nb	15.22	$Nb+Nb_2C$	5.64	$Nb+Nb_2C$
3.28	Nb	7.68	$Nb+Nb_2C$	14.78	$Nb+Nb_2C$
2.73	Nb	13.71	$Nb+Nb_2C$	0	$Nb+Nb_2C$
2.76	Nb	19.98	$Nb+Nb_2C$	3.27	$Nb+Nb_2C$
3.45	Nb	1.64	$Nb+Nb_2C$	13.19	$Nb+Nb_2C$
2.56	Nb	18.81	$Nb+Nb_2C$	2.54	$Nb+Nb_2C$

TABLE I.—CONTINUED.

4T-1-2		4T-3-3		4T-5-2	
C (at.%)	Predicted phases	C (at.%)	Predicted phases	C (at.%)	Predicted phases
2.91	Nb	9.79	$Nb+Nb_2C$	15.59	$Nb+Nb_2C$
2.99	Nb	12.36	$Nb+Nb_2C$	0	$Nb+Nb_2C$
2.59	Nb	19.54	$Nb+Nb_2C$	10.26	$Nb+Nb_2C$
3.02	Nb	12.57	$Nb+Nb_2C$	12.94	$Nb+Nb_2C$
2.47	Nb	11.41	$Nb+Nb_2C$	10.14	$Nb+Nb_2C$
2.82	Nb	20.21	$Nb+Nb_2C$	2.06	$Nb+Nb_2C$
2.73	Nb	18.02	$Nb+Nb_2C$	4.95	$Nb+Nb_2C$
3.41	Nb	0	$Nb+Nb_2C$	0	$Nb+Nb_2C$
3.39	Nb	21.6	$Nb+Nb_2C$	13.22	$Nb+Nb_2C$
2.53	Nb	11.05	$Nb+Nb_2C$	4.53	$Nb+Nb_2C$
2.94	Nb	18.34	$Nb+Nb_2C$	1.91	$Nb+Nb_2C$
2.86	Nb	8.17	$Nb+Nb_2C$	1.18	$Nb+Nb_2C$
3	Nb	4.92	$Nb+Nb_2C$	8.51	$Nb+Nb_2C$
2.84	Nb	12.29	$Nb+Nb_2C$	8.12	$Nb+Nb_2C$
2.96	Nb	0.07	$Nb+Nb_2C$	12.43	$Nb+Nb_2C$
2.03	Nb	8.33	$Nb+Nb_2C$	-------	-----------
2.72	Nb	9.82	$Nb+Nb_2C$	-------	-----------
2.99	Nb	13.04	$Nb+Nb_2C$	-------	-----------
2.85	Nb	6.38	$Nb+Nb_2C$	-------	-----------
2.31	Nb	22.63	$Nb+Nb_2C$	-------	-----------
2.34	Nb	6.26	$Nb+Nb_2C$	-------	-----------
2.61	Nb	9.43	$Nb+Nb_2C$	-------	-----------
2.95	Nb	18.54	$Nb+Nb_2C$	-------	-----------
2.32	Nb	19.71	$Nb+Nb_2C$	-------	-----------
2.7	Nb	11.06	$Nb+Nb_2C$	-------	-----------
3.08	Nb	16.42	$Nb+Nb_2C$	-------	-----------
2.12	Nb	11.73	$Nb+Nb_2C$	-------	-----------
2.74	Nb	9.64	$Nb+Nb_2C$	-------	-----------
2.76	Nb	11.8	$Nb+Nb_2C$	-------	-----------
-----	---	0	$Nb+Nb_2C$	-------	-----------
-----	---	6.35	$Nb+Nb_2C$	-------	-----------
-----	---	19.74	$Nb+Nb_2C$	-------	-----------
-----	---	19.92	$Nb+Nb_2C$	-------	-----------
-----	---	12.2	$Nb+Nb_2C$	-------	-----------
-----	---	10.16	$Nb+Nb_2C$	-------	-----------

TABLE I.—CONCLUDED.

4T-1-2		4T-3-3		4T-5-2	
C (at.%)	Predicted phases	C (at.%)	Predicted phases	C (at.%)	Predicted phases
-----	---	0	Nb+Nb_2C	-------	-----------
-----	---	13.21	Nb+Nb_2C	-------	-----------
-----	---	23.67	Nb+Nb_2C	-------	-----------
-----	---	0	Nb+Nb_2C	-------	-----------
-----	---	18.48	Nb+Nb_2C	-------	-----------
-----	---	5.47	Nb+Nb_2C	-------	-----------
-----	---	0	Nb+Nb_2C	-------	-----------
-----	---	9.44	Nb+Nb_2C	-------	-----------
-----	---	20.61	Nb+Nb_2C	-------	-----------
-----	---	15.36	Nb+Nb_2C	-------	-----------
-----	---	17.28	Nb+Nb_2C	-------	-----------
-----	---	10.69	Nb+Nb_2C	-------	-----------
-----	---	19.08	Nb+Nb_2C	-------	-----------
-----	---	14.37	Nb+Nb_2C	-------	-----------
-----	---	0	Nb+Nb_2C	-------	-----------
-----	---	21.81	Nb+Nb_2C	-------	-----------
-----	---	1.42	Nb+Nb_2C	-------	-----------
-----	---	9.88	Nb+Nb_2C	-------	-----------

Three microhardness Vickers numbers, H_V, measurements made on the NbC layer in channel 4T-3-3 using a 0.1 kg load revealed values of 1556, 1675 and 1675[10]. In contrast, a value of H_V =1268 was observed in the NbC in one of the peripheral channels[11]. Table II compares these values with literature values for Nb [49] and different niobium carbide phases [47,50,51,52]. Clearly, the measured values of H_V of 1556 to 1675 for channel 4T-3-3 with the literature values reported for Nb and NbC_x are higher than those for Nb but not high enough to match the values for NbC_x. Referring to Table I, where the corrected C values predict a range of phases from NbC to Nb+Nb_2C for channel 4T-3-3, there appears to be a qualitative consistency in the expected and observed results. Nevertheless, there is some ambiguity in drawing a firm conclusion based on the current observations and additional electron microprobe (EM) and transmission electron microscopy (TEM) observations are required to confirm this conclusion. In the case of the peripheral channel for which a single H_V value of 1268[12] was measured for NbC layer, this preliminary observation suggests that this layer was not Nb. Although no conclusive can be made based on a single measurement, these preliminary results suggest that this layer has much higher C levels than

---

[10] It is important to note that these values of H_V are cursory measurements conducted to clearly distinguish whether the NbC layer is Nb or NbC. Since only one to three measurements were made, and cracks were generated by the indents, the magnitudes of the H_V reported in this report must be accepted with a degree of caution.

[11] Since the Pt coating used for studying the specimens in the SEM had to be polished off before conducting the microhardness measurements, the reference ink markings used for identifying each channel with respect of the specimen was also obliterated during polishing. So, it was not possible to identify the channel.

[12] It is noted that there was significant cracking around the indentation, which makes this value suspect.

those shown in Table I. Again, it is necessary to evaluate the composition and microstructures of the coating layers with EM and TEM, respectively.

Table III shows the average corrected values of the O levels in the different layers for 4T-1-2, 4T-3-3, and 4T-5-2 specimens. Clearly, O levels are very high in all the layers varying between 5.7 and 46.9 at.%. These observations are consistent with the O levels observed in the coated disk specimens. As noted earlier, the Mo overlay layer was well-bonded to the ZrC layer in the coated disk specimen DS-2 (Figure 10(a) and (b)) with no significant O being detected in the as-received coating (Figure 11(a) to (g)). In contrast, the coated disk specimen DS-1 showed a large amount of O and a debonded Mo overlay layer although the composition analyses were made on thermally-cycled specimens. Clearly, these initial results suggest that there was oxygen ingress into the CVD reactor system during the deposition of the Mo and the Nb layers, which appeared to have influenced its ability to bond with the other layers. Importantly, the corrected O levels were also high in the NbC and the ZrC layers. While the O contamination of the CVD reactor system could have originated from the oxychloride impurities in the precursor metallic salts used for depositing the coatings [42,43], another possibility is a leak in the system since all the layers exhibited high values of O (Table I). A close examination of EDS maps revealed that the O was nonuniformly distributed in the Mo layer and preferentially segregated in a few columnar grains (Figure 20(a), Figure 21(a), and Figure 22(a)).

TABLE II.—COMPARISON OF THE MICROHARDNESS VALUES FOR NB [49] AND NIOBIUM CARBIDE PHASES [47,50,51] WITH THE VALUES MEASURED FOR THE NBC LAYER

C (at.%)	Phase	Room temperature microhardness nos. Knoop (H_K) and Vickers (H_V)	Reference
0	Nb (recrystallized)	60-110 H_V	Plansee [49]
44.5	$NbC_{0.80}$ (single crystal with some Nb_2C precipitates))	2850-3150 H_V	Kumashiro and Sakuma [50]
45.5	$NbC_{0.83}$ (Nb_6C_5 (as-grown single crystal))	2200-2500 H_K	Morgan and Lewis [47]
45.5	NbC (carburized single crystal))	1820-2160 H_K	Morgan and Lewis [47]
------	NbC	1800	Holleck [51]
------	NbC	2004 H_V	Pierson [52]
------	NbC layer (4T-3-3)	1556-1675 H_V	Present investigation
------	NbC layer (4T-peripheral)	1268 H_V	Present investigation

TABLE III.—AVERAGE VALUES OF THE CORRECTED OXYGEN LEVELS IN THE DIFFERENT NOMINAL COATING LAYERS IN THREE CHANNEL OF SECTION 4T OF THE COATED 152.4 mm LONG ROD

Nominal layer composition	O (at.%)[a]		
	4T-1-2	4T-3-3	4T-5-2
NbC	12.2 ± 2.3	8.5 ± 2.2	5.7 ± 2.0
Mo	9.4 ± 1.6	23.0 ± 3.0	30.5 ± 1.9
Nb	25.1 ± 4.4	17.3 ± 3.9	24.5 ± 4.9
ZrC	46.3 ± 2.6	26.4 ± 3.1	26.0 ± 6.0
Mo overlay	46.9 ± 1.9	------------	32.3 ± 2.8

[a] The error limits represent the 95% confidence intervals.

5.0 Summary and Conclusions

A new multilayered coating architecture was proposed to address the “mid-band corrosion” problem observed in Gr-based nuclear fuel elements during the NERVA/Rover NTP programs [23,24]. The proposed coating architecture was Gr/NbC/Mo/Nb/ZrC/Mo. This document reports the results of the initial proof-of-concept studies conducted to demonstrate the ability to deposit these multilayered coatings on Gr disks and inside 19 channels within hexagonal rods 152.4 mm long by CVD. Detailed microstructural observations of the cross-sections of two as-received multilayered coated disks revealed that the outer Mo overlay intact was intact and well-bonded to the ZrC layer in one specimen while it had debonded in the other. Unexpected large amounts of C detected in these specimens in the EDS analyses were partly attributed to hydrocarbon contamination of the specimen surface. Interestingly, the specimen with the debonded Mo overlay layer also had a high oxygen content thereby suggesting that there was a possible correlation between the two observations.

The two coated disk specimens were thermally cycled between ambient and 1900 K with a 1 h hold at the maximum temperature. The specimen with the intact Mo overlay coating was cycled in steps, where the maximum temperature was increased in 100 K increments from 1000 to 1900 K for a total of 19 cumulative cycles. The other specimen with a debonded Mo overlay layer was directly thermally cycled between ambient and 1900 K for 20 cycles with a 1 h hold times at 1900 K. The coatings were intact in both specimens after the thermal cycling experiments although post-test microstructural observations showed that some cracks had propagated from the ZrC layer into the Nb layer below. Also, several horizontal cracks were observed in the NbC layer.

Both μ-CT and microstructural SEM observations of several transverse sections cut along the length of an as-coated 152.4 mm long Gr rod confirmed that all the 19 channels had been coated throughout its entire length. Detailed BSE, SEM, EDS line scans, and EDS maps were conducted on a transverse section, 4T, cut from the middle of the rod, where only the two peripheral channels and a central channel were specifically selected for examination. These observations showed that the Mo overlay had either debonded or was missing. The NbC, Mo, Nb and the ZrC layers were observed. The measured values of C in the EDS lines scans were excessively high and did not correspond with the corresponding EDS maps. Large values of O were also observed, which correlated with the observed debonding of the Mo overlay layer. The probable source of oxygen in the CVD system was attributed to either the vaporization of oxychloride impurities in the precursor salts during CVD or to a pin hole leak in the CVD system.

The high observed values of C in the different coating layers, which predicted duplex microstructures based on the binary Nb-C phase diagram [46], were not consistent with the observed single phase microstructures. An attempt was made to correct the observed C values by assuming that there was no significant C present in the Nb layer since it was further away from the Gr substrate than the Mo layer. The Cl, Mo, Nb, O, and Zr values were also corrected based on the corrected values of C. The corrected elemental line scans were consistent with the observed EDS maps. The corrected C levels were compared with the binary Mo-C, Nb-C and the Zr-C phase diagrams to ensure that there was consistency between the expected and the observed microstructures. While there appeared to be a qualitative agreement for the Mo, Nb, ZrC, and the Mo overlay layers, the outcome was ambiguous for the NbC layer. In the case of the central channel, 4T-3-3, the measured Vickers microhardness values, which were lower than those for NbC_x but higher than that for Nb, were qualitatively consistent with the predicted single and duplex microstructures based on the corrected C line scans of the coating layers. However, the results were inconsistent for the peripheral channels, where the observed single phase microstructure did not agree with predicted duplex microstructure. It is concluded that additional electron microprobe compositional analyses as well as transmission electron microscopy observations will need to be conducted to confirm the results.

References

[1] S. K. Borowski, D. S. R. McCurdy and T. W. Packard, “7-Launch NTR Space Transportation System for NASA’s Mars Design Reference Architecture (DRA) 5.0,” AIAA 2009-5308, 45th AIAA/ASME/SAE/ASEE Joint Propulsion Conference and Exhibit, Denver, CO, American Institute of Aeronautics and Astronautics, Washington, D.C. (2009). https://doi.org/10.2514/6.2009-5308.

[2] S. K. Borowski et al. “Affordable Development and Demonstration of a Small NTR Engine and Stage: Preliminary NASA, DOE and Industry Assessment,” 51st AIAA/ASME/SAE/ASEE Joint Propulsion Conference and Exhibit, Orlando, FL, AIAA 2015-3774, American Institute of Aeronautics and Astronautics, Washington, D.C. (2015). https://doi.org/10.2514/6.2015-3774.

[3] S. K. Borowski *et al*. “Affordable Development and Demonstration of a Small NTR Engine and Stage: How Small is Big Enough?,” Space 2015 Forum & Exposition, Pasadena, CA, AIAA-2015-4524, American Institute of Aeronautics and Astronautics, Washington, D.C. (2015). https://doi.org/10.2514/6.2015-4524.

[4] H. F. Crouch, “Nuclear Space Propulsion,” Astronuclear Press, Granada Hills, CA (1965).

[5] M. J. L. Turner, “Rocket and Spacecraft Propulsion: Principles, Practice and New Developments,” 2nd ed., Springer/Praxis Publishing, Chichester, UK (2005).

[6] T. L. Lawrence, “Nuclear-Thermal-Rocket Propulsion Systems,” edited by C. Bruno, Nuclear Space Power and Propulsion Systems, Progress in Astronautics and Aeronautics, vol. 225, F. K. Lu (Editor-in-Chief), American Institute of Aeronautics and Astronautics, Inc., Reston, VA (2008).

[7] T. C. Wallace, “Chemical Vapor Deposition of ZrC in Small Bore Carbon-Composite Tubes,” LA-UR-73-692, Los Alamos National Laboratory, Los Alamos, NM (1973).

[8] A. J. Caputo, “Characterization of Vapor-Deposited Niobium and Zirconium Carbides,” Nerva Fuel Element Development Program, Summary Report - July 1966 through June 1972, Y1852 Part 3,” Oak Ridge Y-12 Plant, Oak Ridge, TN, September (1973).

[9] A. J. Caputo, “Vapor Deposition of Metal Carbides,” Nerva Fuel Element Development Program, Summary Report - July 1966 through June 1972, Y1852 Part 4,” Oak Ridge Y-12 Plant, Oak Ridge, TN, September (1973).

[10] L. L. Lyon, “Performance of (U,Zr)C-Graphite (Composite) and of (U,Zr)C (Carbide) Fuel Elements in the Nuclear Furnace 1 Test Reactor,” LA-5398-MS, Los Alamos National Laboratory, Los Alamos, NM (1973).

[11] D. R. Koenig, “Experienced Gained from the Space Nuclear Rocket Program (Rover), LA-10062-H,” Los Alamos National Laboratory, Los Alamos, NM (1986).

[12] S. K. Bhattacharya, “An Assessment of Fuels for Nuclear Thermal Propulsion,” ANL/TD/TM01-22, Argonne National Laboratory, Argonne, IL (2001).

[13] K. Benensky, “Tested and Analyzed Fuel Form Candidates for Nuclear Thermal Propulsion Applications,” Nuclear Engineering Reports, University of Tennessee, Knoxville, TN, (2016). https://trace.tennessee.edu/utne_reports/5.

[14] J. S. Clark et al., “Nuclear Thermal Propulsion Technology: Results of an Interagency Panel in FY 1991,” NASA TM 105711, NASA Lewis Research Center (1993).

[15] M. S. El-Genk, “Pellet Bed Reactor for Nuclear Propelled Vehicles: I. Reactor Technology,” in: J. S. Clark (Ed.), Proceedings of the Nuclear Thermal Propulsion Workshop, NASA Conference Publication 10079, NASA Lewis Research Center, Cleveland, OH, pp. 244-261 (1990).

[16] D. P. Butt, D. G. Pelaccio and M. S. El-Genk, "A Review of Carbide Fuel Corrosion for Nuclear Thermal Propulsion Applications," LA-UR-93-4136, Los Alamos National Laboratory, Los Alamos, NM (1994).

[17] M. S. El-Genk, "Nuclear Thermal Propulsion Carbide Fuel Corrosion and Key Issues Final Report," NASA CR 197533, NASA Lewis Research Center, Cleveland, OH (1994).

[18] D. G. Pelaccio, M. S. El-Genk, and D. P. Butt, "Hydrogen Corrosion Considerations of Carbide Fuels for Nuclear Thermal Propulsion Applications," J. Prop. Power, 11, pp. 1338-1348 (1995).

[19] M. P. Trammell et al., "Recapturing Graphite-Based Fuel Element Technology for Nuclear Thermal Propulsion," 49th AIAA/ASME/SAE/ASEE Joint Propulsion Conference and Exhibit, San Jose, CA, AIAA-2013-4159, American Institute of Aeronautics and Astronautics, Washington, D.C. (2013). https://doi.org/10.2514/6.2013-4159.

[20] M. P. Trammell, B. Jolly and A. L. Qualls, "Extrusion Development of Graphite-Based Composite Fuel for Nuclear Thermal Propulsion," 51st AIAA/ASME/SAE/ASEE Joint Propulsion Conference and Exhibit, Orlando, FL, AIAA 2015-3776, American Institute of Aeronautics and Astronautics, Washington, D.C. (2015). https://doi.org/10.2514/6.2013-4159.

[21] B. Jolly, M. P. Trammell and A. L. Qualls, "Coating Development on Graphite-Based Composite Fuel for Nuclear Thermal Propulsion," 51st AIAA/ASME/SAE/ASEE Joint Propulsion Conference and Exhibit, Orlando, FL, AIAA 2015-3777, American Institute of Aeronautics and Astronautics, Washington, D.C. (2015). https://doi.org/10.2514/6.2015-3777.

[22] W. Emrich, "NCPS NTREES Testing Milestone for 2015," Internal report, NASA Marshall Space Flight Center, Huntsville, AL (2015).

[23] S. V. Raj, M. Stewart and J. A. Nesbitt, "Advanced Protective Coatings for Gr-Based Nuclear Propulsion Fuel Elements," U.S. patent 10,068,675 B1, Sept. 4, 2018.

[24] S. V. Raj, "Advanced Multilayer Protective Coatings for Graphite, Graphite-Based and Carbide-Based Substrates," LEW 20116-1, U.S. Provisional Patent Application, June 1, 2020.

[25] S. V. Raj, J. A. Nesbitt, L. Fehrenbacher and D. Carpenter, "Advanced Coatings Development for Nuclear Thermal Propulsion Fuel Elements," NASA TM 2016-218836, NASA Glenn Research Center, Cleveland, OH 44135 (2016).

[26] V. F. Sears, "Neutron Scattering Lengths and Cross Sections," Neutron News, vol. 3, pp. 26-37 (1992).

[27] H. Rauch and W. Waschkowski, "Neutron Scattering Lengths," Neutron Data Booklet (2nd Ed.), edited by A-J. Dianoux and G. Lander, Neutrons for Science, Institute Laue-Langevin, Grenoble, FR (2003). https://www.ill.eu/fileadmin/user_upload/ILL/1_About_ILL/Documentation/NeutronDataBooklet.pdf.

[28] S.F. Mughabghab, "Thermal Neutron Capture Cross Sections Resonance Integrals And G-Factors," INDC (NDS)-440, International Nuclear Data Committee, International Atomic Energy Agency, Vienna, Austria (2003).

[29] Binary Alloy Phase Diagrams (2nd Ed.), vol. 1, edited by T. B. Massalski, H. Okamoto, P. R. Subramanian and L. Kacprzak, ASM International, Materials Park, OH, pp. 899-900 (1990).

[30] Y. S. Touloukian, R. K. Kirby, R. E. Taylor and T. Y. R. Lee, "Thermal Expansion: Nonmetallic Expansion, Thermophysical Properties of Matter," Vol. 13, Plenum, New York, NY (1977).

[31] Y. S. Touloukian, R. K. Kirby, R. E. Taylor and T. Y. R. Lee, "Thermal Expansion: Metallic Expansion, Thermophysical Properties of Matter," Vol. 13, Plenum, New York, NY, p. 208 (1977).

[32] S. V. Raj, unpublished research, Glenn Research Center, Cleveland, OH (2013).

[33] M. D. Holder, private communication, GrafTech International, Brooklyn Heights, OH (2012).

[34] L. Brewer and R. H. Lamoreaux, Binary Alloy Phase Diagrams (2nd Ed.), edited by T. B. Massalski, H. Okamoto, P. R. Subramanian and L. Kacprzak, p. 2634, ASM International, Materials Park, OH (1990).

[35] https://www.graphite-eng.com/uploads/downloads/ Properties_of_Popuar_Mersen_Grades.pdf.

[36] S. Wei, H. Z. Hua and X. Xiang, "Thermodynamic Analysis and Growth of Zirconium Carbide by Chemical Vapor Deposition," Phys. Procedia, 46, pp. 88-101 (2013).

[37] G. Love, V. D. Scott, N. M. T. Dennis and L. Laurenson, "Sources of Contamination in Electron Optical Instruments," Scanning, 4, pp. 32-39 (1981).

[38] P. Hirsch, M. Kässens, M. Pütmann and L. Reimer, "Contamination in a Scanning Electron Microscope and the Influence of Specimen Cooling," Scanning, 16, pp. 101-110 (1994). https://doi.org/10.1002/sca.4950160207.

[39] A. J. V. Griffiths and T. L. Walther, "Quantification of Carbon Contamination Under Electron Beam Irradiation in a Scanning Transmission Electron Microscope and its Suppression by Plasma Cleaning," Electron Microscopy and Analysis Group Conference 2009 (EMAG 2009), Journal of Physics: Conference Series, 241, pp. 1-4 (2010) 012017. doi:10.1088/1742-6596/241/1/012017.

[40] E. G. Il'in et al. "Surface Morphology and Composition of a NbC/C Composite Studied by Scanning Electron Microscopy and X-Ray Photoelectron Spectroscopy," Inorganic Materials, 56, pp. 443-450 (2020).

[41] J. P. Abriata and J. C. Bolcich, Binary Alloy Phase Diagrams (2nd Ed.), vol. 3, edited by T. B. Massalski, H. Okamoto, P. R. Subramanian and L. Kacprzak, ASM International, Materials Park, OH, pp. 2788-2789 (1990).

[42] R. J. M. Konings and A. S. Booij, "Infrared Spectra of NbCl5 and MoCl5 in the Gas Phase," Vibrational Spectroscopy, 6, pp. 345-349 (1994).

[43] S. Harjanto et al., "Thermal Decomposition of NbCl5 in Reductive Atmosphere by Using Hydrogen Gas," Resources Processing, 52, pp. 113-121 (2005).

[44] S. S. Zumdahl, "Introductory Chemistry: A Foundation" (5th ed.), Houghton Mifflin Co., Boston, MA (2004).

[45] CRC Handbook of Chemistry and Physics (61st Ed.), edited by R. C. Weast and A. J. Astle, CRC Press, Inc., Boca Raton, FL (1980).

[46] J. F. Smith, O. N. Carlson and R. R. de Avillez, Binary Alloy Phase Diagrams (2nd Ed.), vol. 1, edited by T. B. Massalski, H. Okamoto, P. R. Subramanian and L. Kacprzak, ASM International, Materials Park, OH, pp. 863-865 (1990).

[47] G. Morgan and M. H. Lewis, "Hardness in Anisotropy in Niobium Carbide," J. Mater. Sci., 9, pp. 349-358 (1974).

[48] Binary Alloy Phase Diagrams (2nd Ed.), vol. 1, edited by T. B. Massalski, H. Okamoto, P. R. Subramanian and L. Kacprzak, ASM International, Materials Park, OH, pp. 899-900 (1990).

[49] https://www.plansee.com/en/materials/niobium.html.

[50] Y. Kumashiro and E. Sakuma, "The Vickers micro-hardness of non-stoichiometric niobium carbide and vanadium carbide single crystals up to 1500 °C," J. Mater. Sci. Lett., 15, pp. 1321-1324 (1980).

[51] H. Holleck, "Materials Selection for Hard Coatings," J. Vac. Sci. Technol. A4, pp. 2661-2669 (1986). https://doi.org/10.1116/1.573700.

[52] H. O. Pierson, "Handbook of Refractory Carbides and Nitrides: Properties, Characteristics, Processing and Applications," Noyes Publications, Westwood, NJ, pp. 55-80 (1996).